

# Multilayers Alkali Metal Structures a Way to High Capacity and Fast Charging Carbon-Based Metal-Ion Battery. A Review

Ilya V. Chepkasov\* and Alexander G. Kvashnin

Recent experiments have revealed that lithium can form multilayer structures when intercalated in bilayer graphene [Nature 564 (2018) 234], challenging the long-held belief that alkali metals in layered materials are confined to single-layer configurations. This pioneering work initiates a new line of research related to the intercalation of alkali metals in carbon-based materials. The possibility of forming multilayer structures between bilayer graphene not only Li but also Na, K, Rb, Cs is shown. Multilayer Li structures are experimentally observed in atomic channels of modified bulk graphite and soft carbon. Multilayer Na structures in the mesochannels of carbon spheres lead to more stable dendrite-free Na cycling with high rate characteristics. It is possible to create fast-charging batteries based on hard carbon, in which the formation of multilayer Na structures in the pores allows to achieve high charging rates. In this review, the achievements in the formation and diffusion of multilayer structures of alkali metals in carbon-based anode materials for creating high-capacity and fast-charging ion batteries are discussed in detail.

## 1. Introduction

Since their inception in the 1970s and subsequent rise to ubiquity in the 1990s, lithium-ion batteries have profoundly reshaped modern society.<sup>[1]</sup> The significance of this breakthrough was cemented in 2019 with the awarding of the Nobel Prize in Chemistry for their development.<sup>[2]</sup> Owing to their high energy density, specific power, long lifetime, and low self-discharge, Li-ion batteries are a paramount renewable energy technology.<sup>[3]</sup> They are the most efficient solution for portable electronics and are pivotal to the electric transport revolution. This role is reflected in the market, with global demand projected to surge from 700 GWh in 2022 to ≈4700 GWh by 2030 a growth overwhelmingly driven by electric vehicles, which are expected to account for ≈4300 GWh.<sup>[4]</sup> Despite their widespread use in applications from portable

I. V. Chepkasov, A. G. Kvashnin  
Skolkovo Institute of Science and Technology  
Bolshoy Boulevard 30, bld. 1, Moscow 121205, Russia  
E-mail: [I.Chepkasov@skoltech.ru](mailto:I.Chepkasov@skoltech.ru)

I. V. Chepkasov  
Katanov Khakas State University  
90 Lenin pr., Abakan 655017, Russia

 The ORCID identification number(s) for the author(s) of this article can be found under <https://doi.org/10.1002/smll.202508433>

DOI: 10.1002/smll.202508433

electronics to electric vehicles, current Li-ion batteries fall short of the growing demand for higher energy density, faster charging, and lower cost. Further improving their design and performance remains a significant challenge.<sup>[5–8]</sup>

The steep rise in lithium prices, driven by high demand for lithium-ion batteries, underscores the urgent need to develop alternatives that utilize more abundant metals and offer superior gravimetric or volumetric energy density.<sup>[9]</sup> Thus, batteries based on sodium (Na),<sup>[10,11]</sup> potassium (K),<sup>[12–14]</sup> rubidium (Rb),<sup>[15]</sup> cesium (Cs),<sup>[16]</sup> magnesium (Mg),<sup>[17,18]</sup> and calcium (Ca)<sup>[19–21]</sup> are increasingly studied due to the high abundance of these elements on Earth and therefore their potentially lower overall cost compared to lithium.

The pursuit of greater battery capacity and energy density has spurred extensive research into next-generation anode materials.<sup>[6,22–37]</sup> In this context, carbon-based materials have garnered significant attention for their low operating potential and ability to reversibly host lithium ions.<sup>[38–42]</sup> Currently, synthetic graphite dominates the anode market, a status owed to its balanced performance in specific capacity and long-term cyclability.<sup>[6,43]</sup>

In the search for anode materials, carbon-based materials seem to be more favorable and commercially viable in the last few decades. Carbon-based electrode materials have high thermodynamic and electrochemical stability compared to other potential anode materials such as metal oxides, chalcogenides, polymers, etc. They are widely available and cost-effective.<sup>[44–48]</sup>

The first commercial Li-ion battery (LIB) introduced by Sony in 1991 used layered electrode materials such as soft carbon as anode and LiCoO<sub>2</sub> as cathode.<sup>[49,50]</sup> The first generation LIB exhibited a high voltage of ≈4 V by using propylene carbonate as the solvent-electrolyte and exhibited a specific energy of 80 Wh kg<sup>-1</sup> (200 Wh L<sup>-1</sup>), which was superior to all other secondary battery technologies available at the time. In the next generation of ion batteries, Sony has replaced soft carbon with hard carbon achieving a higher specific energy density of 120 Wh kg<sup>-1</sup> (295 Wh L<sup>-1</sup>) with an upper cutoff voltage of ≈4.2 V. It was not until the third generation LIB that Sony introduced graphite, which has the advantage of a flatter near-zero potential, as a more efficient anode material.

Graphite prevailed over other anode candidates due to its superior characteristics, including high practical specific capacitance  $\approx 360 \text{ mAhg}^{-1}$  vs. theoretical  $372 \text{ mAhg}^{-1}$ , low operating potential  $\approx 0.1 \text{ V}$  vs.  $\text{Li}^+/\text{Li}$ , stable discharge curve, etc.<sup>[22,46,51,52]</sup> The structure of graphite is well known and consists on hexagonal layers within Bernal (ABA) or rhombohedral ABC stacking.<sup>[53]</sup> This structure is characterized by strong covalent bonding within the graphene planes but weak bonding in the vertical direction, resulting in an interlayer spacing of  $3.35 \text{ \AA}$ , which is well suited for intercalation of guest ions.<sup>[54]</sup> Intercalation of positively charged alkali metal ions into the interlayer leads to the formation of graphite intercalation compounds. The intercalation of alkali metals in graphite has been the subject of extensive research for almost a century, since the initial report on the subject by Freedenhagen and Cadenbach<sup>[55]</sup> in 1926. The intercalation potential is in close proximity to the redox potential of the alkali metals themselves, rendering graphite intercalation compounds attractive anodic materials with mixed ionic and electronic conductivity. The precise structure of graphite intercalation compounds is contingent on the concentration of alkali metals; however, the general layered structure is retained, thereby facilitating 2D conductivity. The intercalation charge storage mechanism in batteries minimizes structural changes in the electrode material, a critical factor in ensuring exceptional longevity.<sup>[56–58]</sup> In other types of anodes, the situation is different, large volumetric changes occur during charging and discharging, leading to electrode failure, since these anodes are based on alloy- or conversion-type reactions.<sup>[59–63]</sup> Thus, graphite's position as the anode of choice for intercalation-based batteries is well-founded, owing to its exceptional structural stability and enduring performance. However, research is constantly being conducted to develop higher-capacity anode materials.<sup>[43,64–67]</sup>

One of the directions of development in order to increase the capacity and charging rate is the modification of carbon-based anodes to form multilayer alkali metal structures in these anodes. Contrary to the widespread consensus that alkali metal (AM) intercalation in layered materials yields only single-layer structures, the pioneering work of Kuhle et al.<sup>[28]</sup> in 2018 revealed that multi-layer lithium configurations are possible in bilayer graphene.

This pioneering work initiated a new line of research related to the intercalation of alkali metals in carbon-based materials, see Figure 1a. In 2020 Chepkasov et al.<sup>[27]</sup> studied the energetics of different AMs (Li, Na, K, Rb, Cs) in bilayer graphene by using first-principles calculations. The negative formation energy of multilayer K, Rb, and Cs structures between graphene sheets confirms their thermodynamic favorability. A lower tendency to form multilayer structures has been shown for Li and Na with slightly positive formation energies. In 2022 Zhou et al.<sup>[68]</sup> studied the formation and diffusion of lithium multilayer structures in atomic channels of modified bulk graphite. In 2023 Ye et al.<sup>[69]</sup> showed that the introduction of open mesochannels in carbon spheres leads to a more stable dendrite-free cycling of Na with high rate properties due to the formation and diffusion of Na multilayer structures through the mesochannels of the carbon sphere. Much more progress has been made in 2024. Li et al. succeeded in creating fast charging hard carbon-based batteries where the formation of Na multilayer structures in the pores allowed them to achieve high charging rates. Wang et al.<sup>[70]</sup> demon-

strated that Li multilayer structures were formed in modified soft carbon with extended interlayer spacing, resulting in suppression of Li dendrite growth and improvements in rate performance. Suenaga et al.<sup>[71]</sup> demonstrated the formation of multilayer structures of K, Rb, Cs between graphene layers, which was predicted theoretically by Chepkasov et al.<sup>[27]</sup>

The primary aim of this review is to consolidate and analyze significant recent advancements in the understanding of the formation and functionality of multilayer alkali metal structures within various carbon-based anode hosts. We will critically examine how this phenomenon, which challenges the conventional single-layer intercalation model, directly enables the development of high-capacity batteries with fast charging capabilities. The discussion will systematically progress from the fundamental discovery of bilayer graphene to its extension into engineered carbon architectures, including graphite with atomic channels, hard carbon, soft carbon, and carbon spheres. By synthesizing insights from these diverse systems, this review seeks to establish a unified understanding of how multi-layer intercalation governs superior ion transport and storage, thereby charting a course for the rational design of next-generation, high-performance metal-ion batteries.

## 2. Bilayer Graphene

### 2.1. Li Inside Bilayer Graphene

All studies devoted to the intercalation of Li (or other AMs) into bulk and few-layer systems since initial report by Freedenhagen and Cadenbach<sup>[55]</sup> in 1926, including Refs. [72–74] assumed that intercalated atoms are formed a single layer between the graphene sheets forming a  $\sqrt{3}x\sqrt{3} \text{ R}30^\circ$  lattice, as shown in Figure 2a. However, Smet et al.<sup>[28]</sup> observed unexpectedly dense Li multilayers between graphene sheets by using *in situ* transmission electron microscopy (TEM, which is one of the most powerful techniques for gaining insights into the dynamics of various processes in energy materials with atomic resolution<sup>[75]</sup>) as shown in Figure 2b,c. Observation of Li multilayers suggests possibility of increase in areal Li storage capacity. The experimental setup is illustrated schematically in Figure 2d, comprised the deposition of bilayer graphene on a substrate with a central hole in the chip, which was then contacted by several metallic electrodes. Such a configuration enabled the measurement of the resistivity of the device, exhibiting distinct variations in the presence and absence of intercalated Li atoms (see Figure 2e). The Li-ion conducting electrolyte (yellow color in Figure 2e) was employed to establish a connection between the bilayer graphene and a metallic counter electrode, thereby forming an electrochemical cell. The presence of a hole in the substrate facilitated *in situ* TEM observations of the lithiation and delithiation processes revealing a dense network of Li atoms (Figure 2c), which was not consistent with the previously reported  $\sqrt{3}x\sqrt{3} \text{ R}30^\circ$  arrangement of atoms (Figure 2a). These observations were explained through the formation of close-packed multilayer structures of Li in the interlayer space (Figure 2b,c). The experiments confirmed that lithiation occurs exclusively between the graphene layers. This was further validated by a control experiment where lithium placed on top of a single layer showed no displacement effect.<sup>[76]</sup>

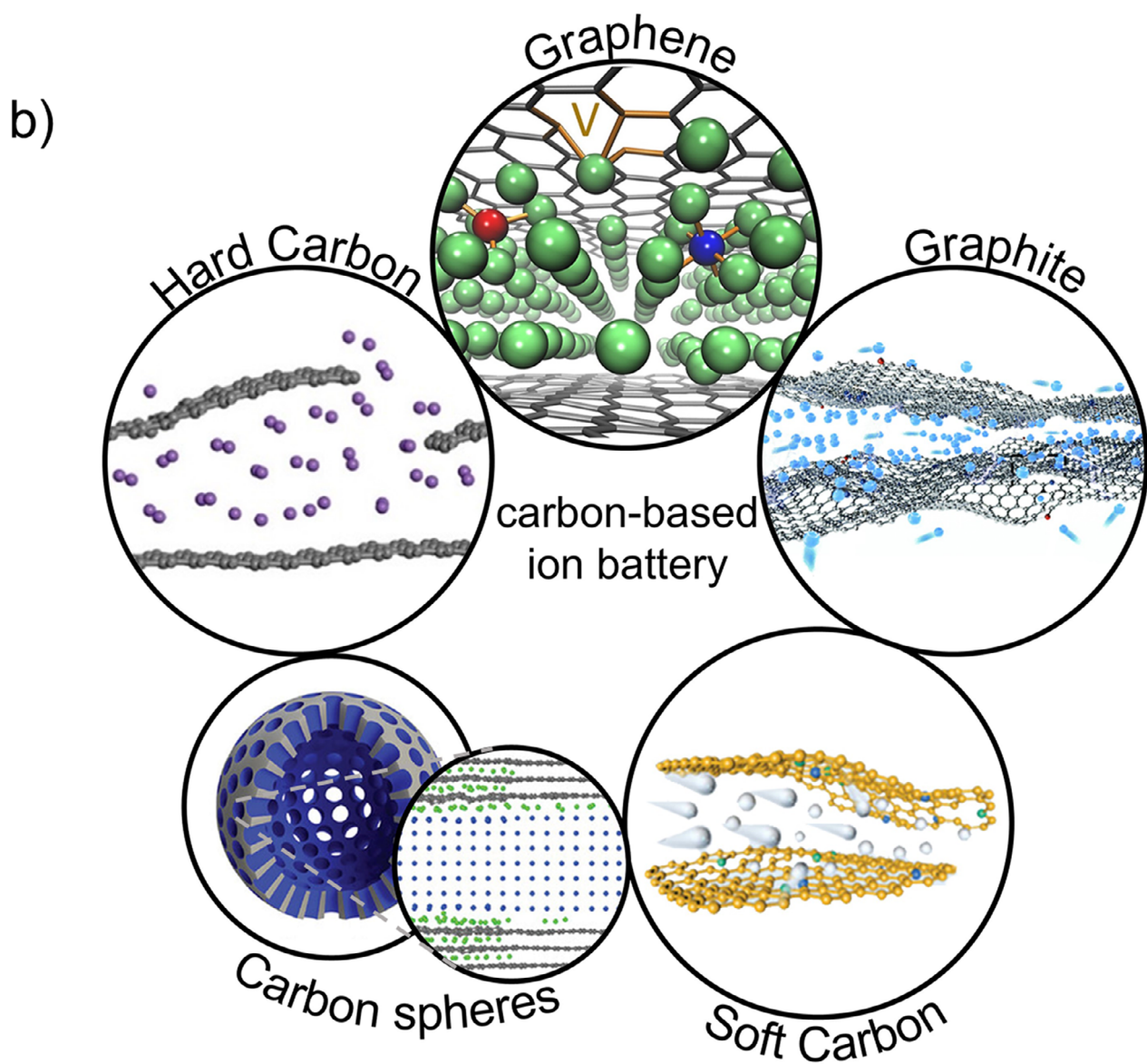
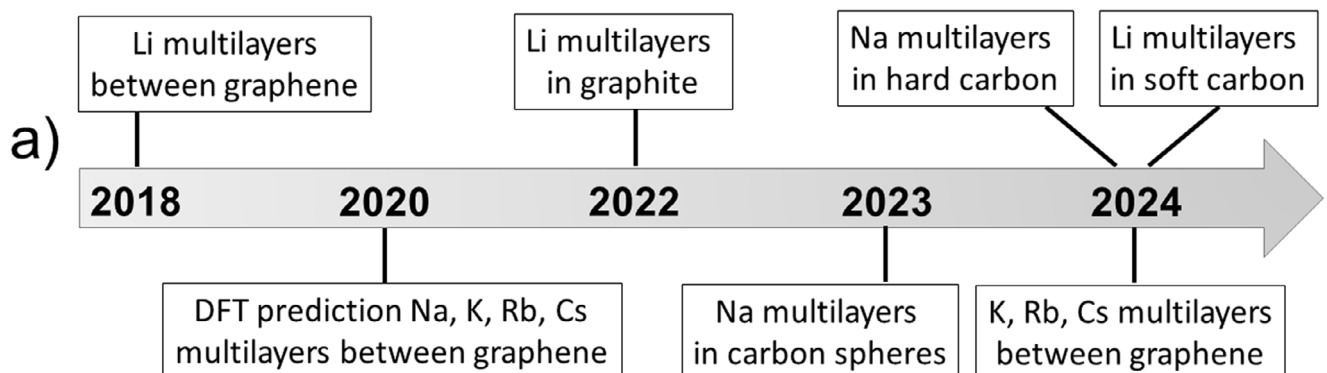


**Figure 1.** a) Timeline of key developments related to multilayers of AMs into carbon-based materials. b) Illustration of the structures multilayers of AMs into carbon-based materials.

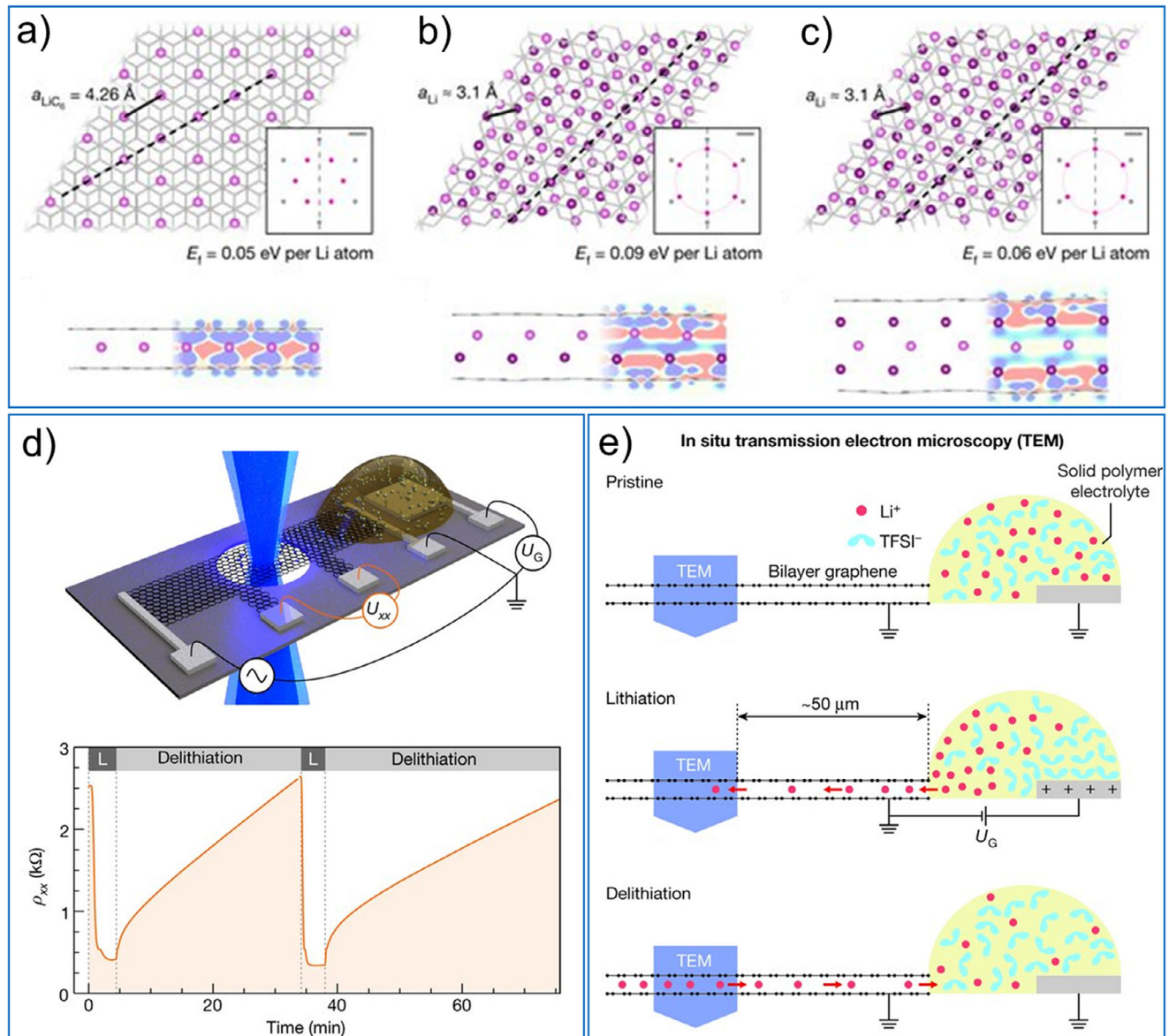


**Figure 2.** a–c) The positions of atoms are consistent with the multilayer Li fcc structure. d) Schematic of the device used in the in situ TEM experiments where multilayer Li structures were formed inside BLG and bilayer graphene resistivity measured in situ during two lithiation/delithiation cycles inside the TEM, schematically illustrated in panel (e). Reproduced and adapted with permission.<sup>[28]</sup> 2018, Springer Nature.

In bilayer graphene, lithium was observed to form an ultra-thin, super-dense close-packed phase with a lattice parameter of  $3.1 \text{ \AA}$ . This unique phase is facilitated by the ability of the two graphene layers to expand their interlayer distance, a volumetric adjustment that is mechanically constrained in bulk graphite by the rigidity of its multi-layer structure.

The nucleation of Li crystals at the early stages of lithiation was observed by Kaiser et al.<sup>[77]</sup> and determined that the nucleation occurs on graphene vacancies, see Figure 3. According to DFT (density functional theory) calculations, the presence of undercoordinated atoms at graphene vacancies enhances Li-graphene interactions, confirming these defects act as nucleation sites for Li crystal growth (Figure 3f). DFT calculations determined the Li adsorption energy on a single vacancy

to be  $-2.78 \text{ eV}$ , representing a significant energy gain  $\approx 1.7 \text{ eV}$  over adsorption on pure graphene. While double vacancies also enhance Li-graphene binding, single vacancies provide the most energetically favorable site.<sup>[78]</sup> A detailed study of the dense close-packing structure of Li crystal formed between graphene sheets showed that Li forms a fcc lattice with ABC stacking (Figure 3a,d), which was confirmed by DFT calculation (Figure 3e).

In addition to the vacancy in graphene, individual atomic defects inside the forming Li crystal were also observed by using high-resolution transmission electron microscopy (HRTEM). This defective atom was identified as oxygen, originating from either the electrolyte or the oxygen-containing lithium metal counter electrode. DFT calculations<sup>[77]</sup> revealed that oxygen

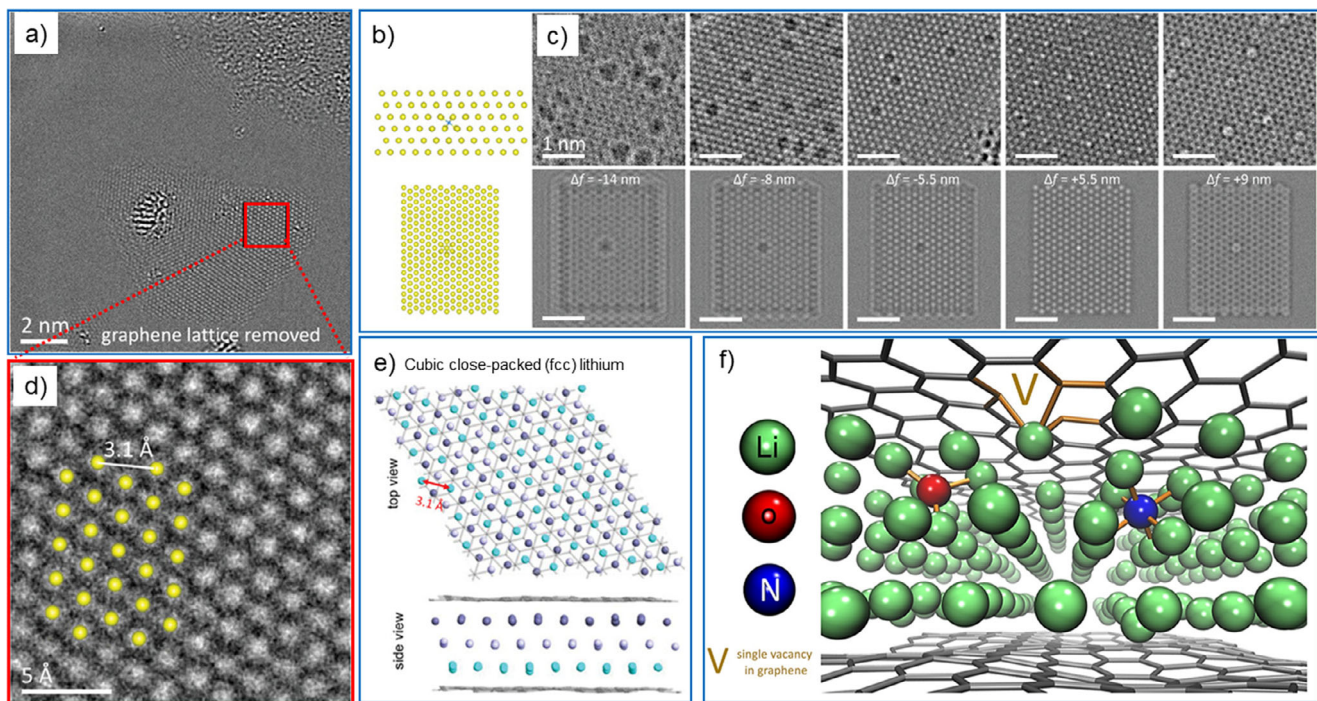


**Figure 3.** a) Atomically resolved TEM image of a triangular Li crystal with graphene lattice removed. b) Atomic model of an O atom at the octahedral interstitial position inside fcc Li relaxed by the DFT optimisation, with the side view above and the top view below. c) Experimental HRTEM images containing O atoms recorded with different defoci and the corresponding simulated images (electron dose  $1 \times 10^5 e^- \text{ Å}^{-2}$ ) using the model in (b) as input. d) Magnified view of the boxed area in panel (a). e) The top view and the side view of the configuration of fcc Li. f) Atomic configurations multi-layer structures of Li between graphene sheets. a–e) Reproduced with permission.<sup>[77]</sup> 2024, John Wiley & Sons, Inc. (f) Reproduced with permission.<sup>[30]</sup> 2023, Elsevier.

atoms are preferentially incorporated into the Li crystal lattice rather than occupying the interface between the graphene and the Li slab. This behavior is analogous to the implantation of carbon atoms into copper foils.<sup>[79]</sup> Oxygen occupy octahedral interstitial position in the Li crystal. The atomic model with an O atom in octahedral interstitial position is shown in Figure 3b. Experimental HRTEM images recorded with different defoci containing the interstitial O atoms are presented in Figure 3c. Krasheninnikov et al.<sup>[30]</sup> performed additional DFT calculations of Li crystals between bilayer graphene with other types of impurities such as N, F and S atoms and showed that all these atoms as well as oxygen occupy octahedral interstitial positions in Li crystals (Figure 3f). Adatoms strongly interact with atoms in the Li crystal thereby preventing the delithiation process. Since the oxygen defects are always inside the Li crystal and never observed near the crystal edge, only intrinsic graphene defects, such as vacancies, determine the shape of the Li crystal formed during lithiation and delithiation (as the crystal shape is determined by the graphene-Li edge and interface energies). Analysis of HRTEM images of Li crystals shows that one of the (111) Li surfaces is orientated parallel to the graphene sheets (Figure 4). This is a noteworthy finding, given that calculations have revealed<sup>[80,81]</sup> that the Li (111) surface has the highest energy and is the least energetically favorable to form. However, considering the energy of graphene-Li(111) interface one can note that this interface is energetically the most favorable compared to others,<sup>[77]</sup> see Figure 4a. The sum of the interface and surface energies for the graphene-Li(111) interface is the lowest, indicating that this type of interface should form.

Thus caused by the fcc structure the edges of formed Li crystal should be faceted by the (100) surfaces, see Figure 4b, which have the lowest formation energy. The growth of triangular-shaped Li clusters with (111) surface and (100) edges as show in Figure 4b is clearly observed during the lithiation process using HRTEM (Figure 4c).

Thus, in a series of works by Kaiser and Krasheninnikov et al.<sup>[28,30,77]</sup> it was shown that it is possible to obtain close-packed lithium multilayers between graphene sheets and that Li crystals nucleate on carbon vacancies in graphene and grow further showing well-formed facets. It was also found that the Li crystals have an fcc structure with single impurity oxygen atoms (as well as possibly N, S and F) within the Li crystals, interacting strongly with the Li atoms and thus hindering the delithiation process.

## 2.2. Theoretical Calculations of Alkali Metals Inside Bi-Layer Graphene

Building on experimental work demonstrating reversible lithium intercalation in bilayer graphene,<sup>[28]</sup> Chepkasov et al.<sup>[27]</sup> conducted a systematic computational study of the intercalation energetics for various alkali metals (Li, Na, K, Rb, Cs). Their investigation considered both the AB and AA stacking configurations of bilayer graphene (BLG). Although the AA stacking is slightly higher in energy ( $\approx 10$  meV per atom), both configurations are experimentally feasible and were therefore included in the analysis.<sup>[82,83]</sup>

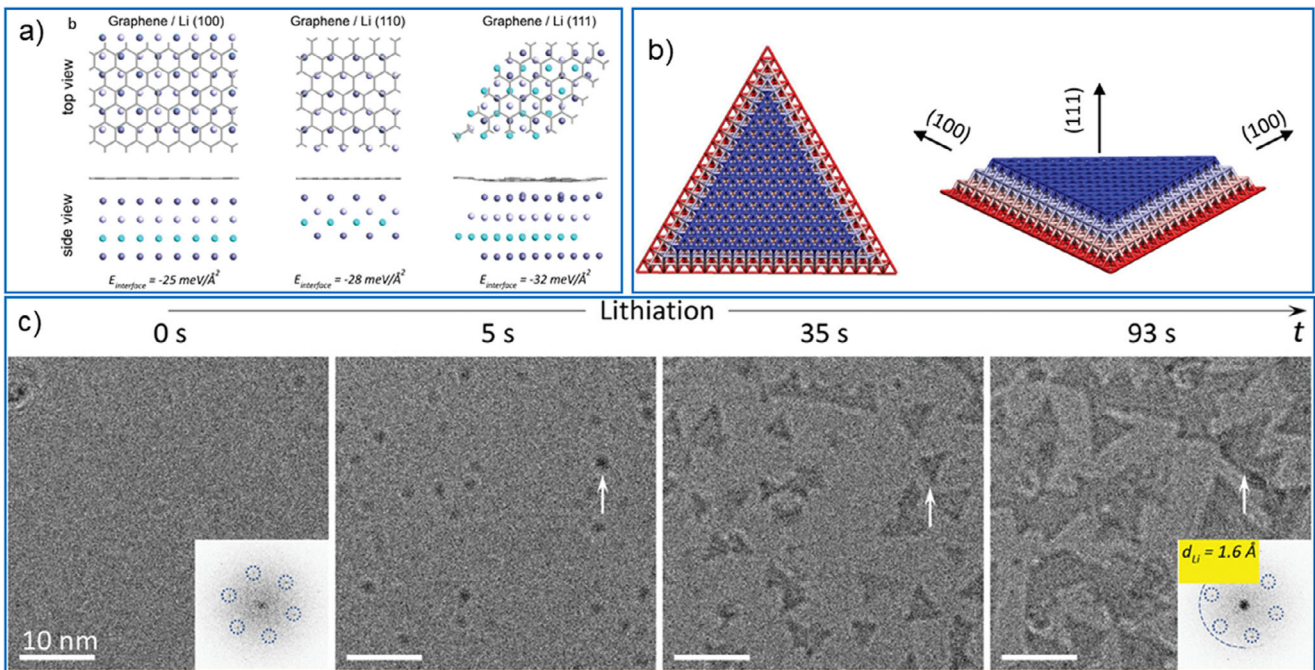


**Figure 4.** a) The simulation model of the graphene/Li (111) interface was constructed using a  $5 \times 5$  graphene supercell on top of a (111)  $4 \times 4 \times 4$  Li slab, with a total strain of  $\approx 0.47\%$ , containing 114 atoms. For the graphene/Li (100) interface, the structure includes using a  $7 \times 2$  graphene supercell on top of a (100)  $4 \times 2 \times 4$  Li slab, with a total strain of  $\approx 0.54\%$ , containing 60 atoms. In the case of graphene/Li (110) interface, the model represents a  $5 \times 2$  graphene supercell on top of a (100)  $4 \times 2 \times 4$  Li slab, with a total strain of  $\approx 0.68\%$ , including 36 atoms. b) Top view and perspective view of a triangular Li cluster. The Li atoms are coloured according to their z-coordinate. c) A series of TEM images showing the first-cycle lithiation process in bilayer graphene. A large underfocus is used to increase the contrast of the Li crystals. Before the lithiation ( $t=0$  s), the inset Fourier transform shows only graphene reflections. Li crystals start to nucleate at  $t=5$  s. From 35 to 93 s, the Li seeds grow into larger faceted plates. The arrows mark the same Li crystal. The inset Fourier transform of the image recorded at  $t=93$  s shows the reflections of a super dense Li phase (marked by the half ring, representing a real-space periodicity of  $1.6 \text{ \AA}$ ). Reproduced with permission.<sup>[77]</sup> 2024, John Wiley & Sons, Inc.

Different structures of AMs were placed between graphene sheets as single and multilayer structures (Figure 5a). For all AMs except Na the formation energy ( $E_f$ ) was negative for one AM layer in AA-stacked graphene, Figure 5b. A similar trend is observed for AB-stacked bilayer graphene, though with slightly higher formation energies due to the asymmetric arrangement of carbon atoms relative to the intercalated alkali metals. In general, forming multilayer alkali metal structures is less favorable than forming single layers, with the notable exception of sodium. For most metals, the formation energy remains negative but increases (becomes less stable) with each additional layer. For sodium, the formation energy becomes positive for two and three layers, yet these values are comparable to those of lithium. Since multilayer lithium structures have been experimentally realized,<sup>[28]</sup> this suggests that multilayer sodium structures should also be feasible. For potassium, rubidium, and cesium, the increasing positive trend in formation energy with layer count makes intercalation less favorable, though still theoretically possible as the energies remain negative. Ultimately, as the number of alkali metal layers grows, the formation energy should approach zero, corresponding to a bulk metal crystal between graphene sheets. Furthermore, unlike single-layer structures, these multilayer systems become incommensurate with the graphene lattice, as the alkali metal spacing is dictated by its own bulk crystal structure rather than just its interaction with the graphene host.

To evaluate charge transfer during intercalation in bilayer systems and compare it with bulk materials, the electron density difference between the combined and separated systems was calculated. Figure 5a presents the resulting charge differences for one, two, and three layers of AM atoms. The plots reveal a significant accumulation of electron density between the Li atoms and the graphene, indicating a strong covalent component to the binding, particularly for a single Li layer. This electron overdistribution remains equally pronounced in double and triple layers (Figure 5a). Consequently, the Li-host interaction is strong even in multilayer structures, and it induces a redistribution of electron density among the Li atoms themselves, enhancing the “covalent” character of the Li-Li bonding.

Charge difference analysis reveals an accumulation of electron density between Li atoms and graphene, pointing to a significant covalent component in the binding, especially for a single Li layer. This pronounced electron redistribution persists in double and triple layers, indicating a consistently strong Li-host interaction. This interaction is so strong that it redistributes electron density among the Li atoms themselves, enhancing their mutual bonding. Furthermore, the overall charge transfer from the AM atoms to the host increases from Na to Cs, mirroring the trend observed in single-layer intercalation (Figure 5a). Analysis reveals that the outer AM atoms, oriented toward the host material, are the primary source of electron loss, while inner atoms (e.g., in the triple layer) largely retain their charge. However, quantifying

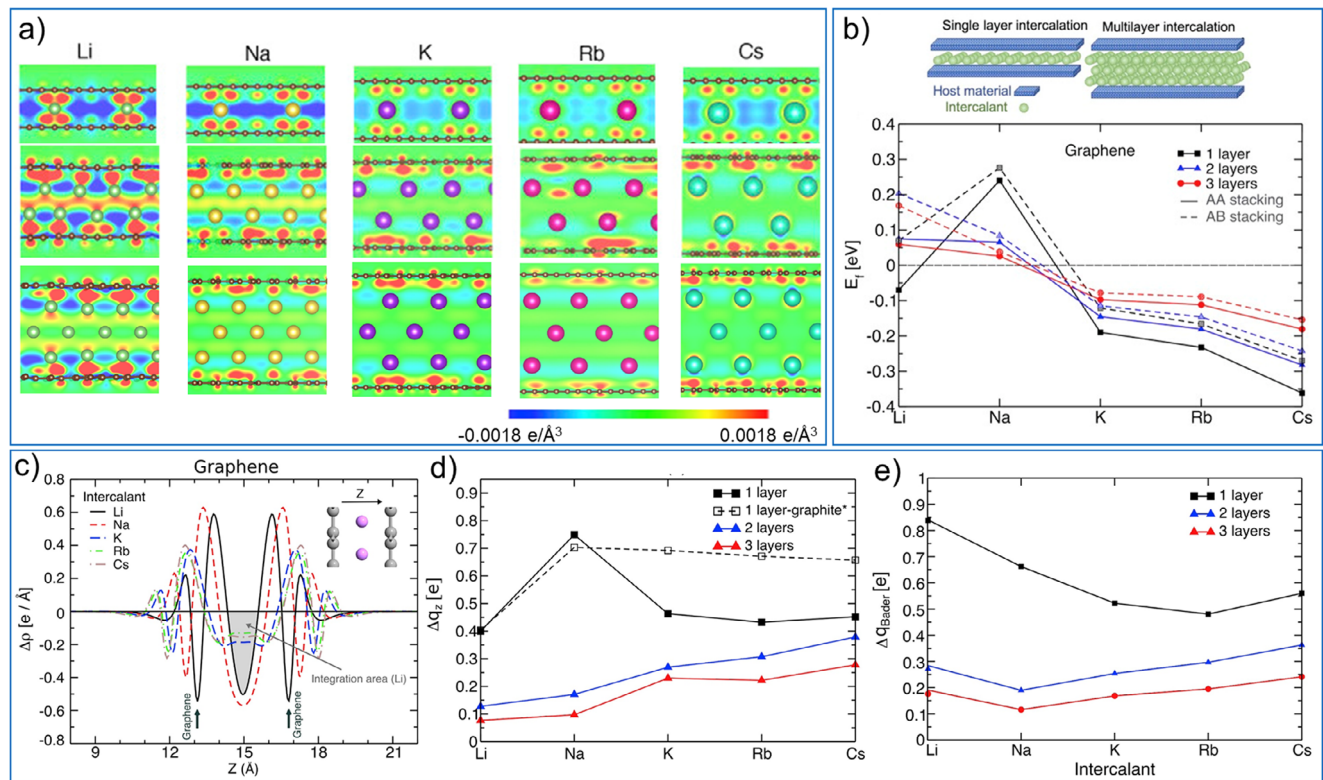


**Figure 5.** a) Charge difference (cross-section through AM atoms perpendicular to the host material planes) for one, two and three layers of AM atoms in bi-layer graphene. Red color corresponds to density build-up, blue to depletion. Note a build-up of the electron density between Li atoms and graphene, illustrating a substantial contribution to the bonding from covalent interaction. b) Formation energy of single layers and multi-layers of AMs (Li, Na, K, Rb, Cs) between AA- and AB-stacked bi-layer graphene. c) Electron density difference  $\Delta\rho$  for single layers of AM atoms averaged in the planes parallel to the graphene sheets as a function of the z-coordinate (perpendicular to the planes). The geometry is schematically shown in the inset. d) Total charge transfer  $\Delta q_z$  for single- and double-layers of AM atoms obtained by integrating over the range of z where, as illustrated for Li in panel (a). The results for a single layer of AM atoms in bulk graphite are also shown. The data for graphite is taken from ref. [84]. e) Charge transfer for single and multi-layer structures as calculated using the Bader method. Reproduced with permission, [27] 2020, Elsevier.

this charge transfer is nontrivial, as the results are sensitive to the computational method used.<sup>[84]</sup> The Bader analysis<sup>[85,86]</sup> is a common method employed for this issue. This analysis is based on determining extrema in the electron density and partitioning space into atomic volumes, respectively. However, it should be noted that Bader charge analysis takes into account the geometric charge transfer that occurs in each system when atoms are added, even in the cases where there is no physical charge transfer between the host and the added atoms.<sup>[84]</sup> Chepkasov et al.<sup>[27]</sup> analyzed the charge transfer between AM layers and graphene by two methods, namely the Bader charge method and by using the averaging  $\Delta\rho$  in planes parallel to the sheets of the base material along the z-axis, as shown schematically in the inset of Figure 5c. The charge difference for one AM layer between graphene sheets is shown in Figure 5c. One can see that the electron density is depleted in the AMs plane and significantly increases in the region between the graphene sheets and AM metals, especially for Li and Na. In Figure 5d, the charge transfer  $\Delta q_z$  is obtained by integrating the region where  $\Delta\rho$  is negative, as shown in Figure 5c for Li by gray color. For a single layer of Li and Na atoms, when the covalent interaction is strong and the atomic radii are small, the results for bilayer graphene are close to the data for bulk graphite.<sup>[84]</sup> For multilayer AM, the charge

transfer increases from Li to Cs, see Figure 5d. The charge transfer analyzed by the Bader method is presented in Figure 5e and give qualitatively (and even quantitatively for all AM, with the exception of Li) the same results for double and triple layers of AM atoms. A detailed analysis of the nature of the chemical bonding between graphene and AM showed that when moving from Li to Cs, the bonds between AM and carbon atoms become less and less covalent.<sup>[27]</sup> This is confirmed by calculated redistribution of electron density shown in Figure 5a and was previously observed during the intercalation of AM into graphite.<sup>[87,88]</sup>

Using the calculated geometries for multilayer AMs in bilayer graphene, the theoretically achievable capacitance of such systems was estimated, shown in Table 1. Theoretical capacitance of trilayer was found to be 828 mAhg<sup>-1</sup> and 440 mAhg<sup>-1</sup> for Li and Na structures, and 1020 and 521 mAhg<sup>-1</sup> for the fourlayer Li and Na structures, respectively. This indicates that the capacitance of bilayer graphene with intercalated multilayer Na structures can exceed the capacitance of graphite with Li. Moreover the capacitance of fourlayers Li is 3 times higher then that of graphite with Li (372 mAhg<sup>-1</sup>).<sup>[27]</sup>

Thus, the first-principles calculations by Chepkasov et al.<sup>[27]</sup> on the intercalation of alkali metals (Li, Na, K, Rb, Cs) in bilayer graphene revealed an energetic preference for forming

**Table 1.** Capacity of the systems with multilayer AMs in bilayer graphene in  $\text{mAhg}^{-1}$ . The structures with capacity close to the theoretical capacity of graphite of  $372 \text{ mAhg}^{-1}$  marked by green.<sup>[27]</sup>

	Li	Na	K	Rb	Cs
1 layer	177	160	146	116	96
2 layers	595	335	214	142	105
3 layers	828	439	277	173	125
4 layers	1020	521	326	200	140

multilayer structures of K, Rb, and Cs. In contrast, multilayer formations of Li and Na are less preferred, exhibiting small positive formation energies. However, the experimental observation of multilayer lithium structures<sup>[28]</sup> suggests that similar formations for sodium are feasible despite being energetically unfavorable. This finding is particularly significant given recent advances in mass-producing bilayer graphene<sup>[23]</sup> and the low cost of sodium, key factors for developing viable Na-ion batteries based on nanosstructured 2D materials.

### 2.3. K, Rb, Cs Inside Bi-Layer Graphene

Suenaga et al.<sup>[71]</sup> employed low-voltage scanning transmission electron microscopy (LV-STEM) to study the vapor-phase intercalation of K, Rb, and Cs into bilayer graphene. Unlike electrochemical methods,<sup>[28]</sup> this vapor-phase approach provides a 'clean' process that enables direct atomic-scale visualization of the intercalated structures. Their analysis revealed that all three AMs consistently form a bilayer configuration with *hcp* stacking within the graphene interlayer; no single- or triple-layer AM structures were observed. For cesium, the bilayer configuration consists of two distinct domains, as shown in Figure 6a. The upper domain exhibits a standard hexagonal arrangement with a Cs-Cs distance of 0.25 nm, consistent with the  $\text{C}_6\text{Cs}_2\text{C}_6$  model (Figure 6f). In striking contrast, the lower domain is highly compressed, with a remarkably short Cs-Cs distance of just 0.14 nm a reduction of nearly 56% in one direction. Such a severe distortion is highly unusual for a monolayer system under equilibrium conditions without external strain. The study identified multiple such intercalated Cs domains with non-equivalent atomic distances. Furthermore, *in situ* STEM imaging captured the migration of these domains, which is explained by the relative displacement of two separate Cs lattices. This indicates a separation of the two Cs layers along the c-axis, as illustrated in the model in Figure 6e. The same *hcp* bilayer arrangement, forming a  $\text{C}_6\text{M}_2\text{C}_6$  structure, was also confirmed for intercalated K and Rb (Figure 6g-i). An enhanced EELS system with a monochromatic electron source was used to quantitatively measure the transport of charge carriers from bilayer AMs to graphene. The measurements yielded that the negative charge transported from the AM structure to the graphene layers is  $\approx 1-1.5 \times 10^{14} \text{ e}^- \text{ cm}^{-2}$ .

DFT geometry optimizations confirm that bilayer structures are the energetically preferred configuration for K, Rb, and Cs intercalated in BLG, as they exhibit a lower energy than their monolayer counterparts (Figure 7). This is exemplified by Cs, whose intercalation dramatically expands the BLG interlayer spacing from 3.4 Å in pristine BLG to 5.95 Å with a single Cs layer, and further

to 11.25 Å with a Cs bilayer. Within this confined geometry, the Cs atoms form a *hcp* structure. The spatial constraint suppresses lateral movement, resulting in a distorted hexagonal pattern where the Cs atoms appear dimerized. This *hcp* bilayer is structurally analogous to the [111] orientation of the *fcc* phase of bulk Cs under high pressure.<sup>[89–92]</sup> Indeed, the calculated shortest Cs-Cs distance in this bilayer is 2.44 Å, a value nearly identical to that found in bulk Cs under pressures of 2.37–4.3 GPa, where the *bcc*-to-*fcc* transition occurs.<sup>[93–95]</sup> This agreement confirms that the interlayer confinement in BLG stabilizes a 2D high-pressure phase. Furthermore, charge redistribution upon intercalation renders each Cs layer partially positive. The resulting electrostatic repulsion increases the interlayer spacing between the two Cs sheets to 5.02 Å, which in turn contributes significantly to the overall expansion of the BLG gallery. The energetic preference for this bilayer configuration over a three-layer structure for K, Rb, and Cs is further supported by recent theoretical studies.<sup>[27]</sup>

Inspired by the results of intercalation of alkali metals (AM) into graphene Suenaga et al.<sup>[71]</sup> studied the intercalation of AM into graphite in more detail. Cross-sectional scanning transmission electron microscopy (STEM) image of Cs intercalated highly-oriented pyrolytic graphite (HOPG) is shown in Figure 8a. Electron energy loss spectroscopy (EELS) mapping overlaid onto the annular dark-field (ADF) cross-sectional image shown in Figure 8b. The Cs signal was found to be widely distributed in the graphite layers with a distinct dark contrast layer displaying a significant Cs signal. A bilayer intercalated Cs structure was observed in the dark contrast region, extending the interlayer graphite spacing to 1.09 nm, in agreement with the model derived from DFT calculations.<sup>[71]</sup> In deeper HOPG layers, single-layer intercalated Cs structures were visualized, extending the interlayer graphite spacing to 0.6 nm. Schematic illustrations of the intercalated structure are shown in Figure 8c,d. The pink regions represent domains with well ordered  $\text{C}_6\text{M}_2\text{C}_6$  structures. At the side, small bilayer AM domains are surrounded by graphite layers. It has been shown experimentally that bilayer AM can intercalate small layers of graphite, which is promising for increasing battery capacity.

While the intercalation of K, Rb, and Cs into bilayer graphene is structurally well-founded and offers intriguing possibilities for high-capacity anodes, the practical development of Rb/Cs-ion batteries remains in its infancy. Overcoming the formidable electrochemical and economic challenges will require focused efforts in materials design, electrolyte chemistry, and fundamental electrochemistry.

### 2.4. Alkali Metals in Graphene/MoS<sub>2</sub>

As demonstrated in the theoretical work of Chepkasov and Krashenninnikov,<sup>[29]</sup> not only bilayer graphene but also multilayer alkali metal structures can form in graphene/MoS<sub>2</sub> heterostructures. Van der Waals (vdW) heterostructures combining graphene with transition metal dichalcogenides (TMDs) like MoS<sub>2</sub> have garnered significant interest due to their potential as high-performance anode materials.<sup>[96–103]</sup> Despite low electronic conductivity of MoS<sub>2</sub> and significant volume changes during intercalation/deintercalation, alkali metal (AM) intercalation in these systems is energetically more favorable

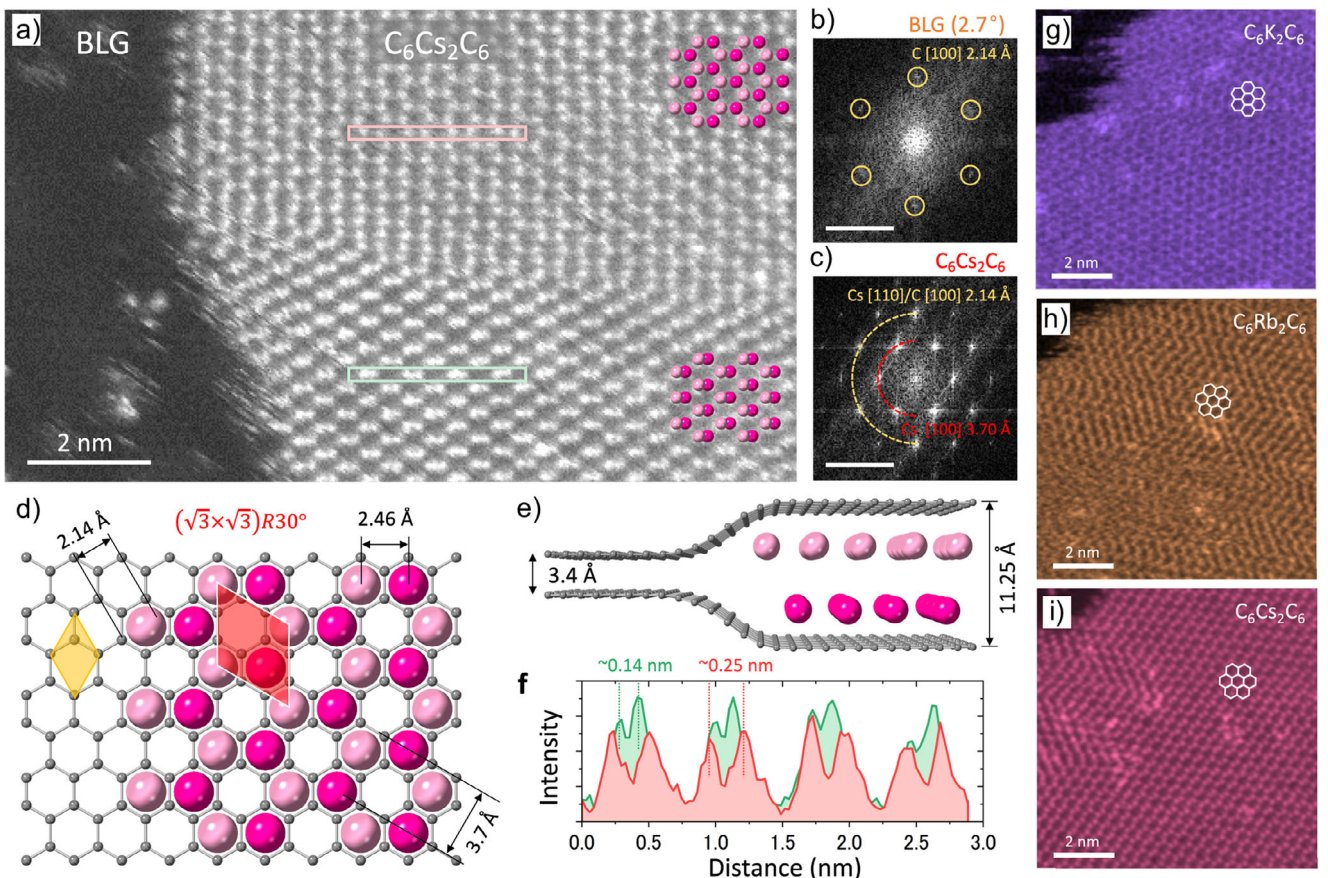


**Figure 6.** a) A STEM annular dark-field (ADF) image of Cs-intercalated BLG displaying the C<sub>6</sub>Cs<sub>2</sub>C<sub>6</sub> structure. b,c) Fast Fourier transform (FFT) image of BLG and Cs domains in (a) (scale bar=5 nm<sup>-1</sup>). BLG exhibits a twist angle of 2.7° between its two graphene layers. The [100] and [110] spots of C<sub>6</sub>Cs<sub>2</sub>C<sub>6</sub> domain correspond to interplanar d-spacings of 3.70 Å and 2.14 Å in real space, with the Cs [110] spots overlapping with the graphene [100] spots. d) Top-view atomic model of C<sub>6</sub>Cs<sub>2</sub>C<sub>6</sub>. The yellow rhombus highlights a graphene (1x1) unit cell with a=b=2.46 Å, while the red rhombus highlights the unit cell of the Cs lattice with lattice, where a=b=4.26 Å. e) Side and perspective view of the C<sub>6</sub>Cs<sub>2</sub>C<sub>6</sub>. The Cs atoms in different atomic planes are color-coded with two different shades of red. f) ADF profile of the hexagonal Cs layer along the pink and light green boxes in (a). The red profile displays the shortest distance between two Cs atoms as 0.25 nm, consistent with the atomic model shown in (d). The green profile shows the shorter distance between the Cs atoms, indicating the lateral displacement of the two Cs atomic planes. g–i) ADF image of C<sub>6</sub>K<sub>2</sub>C<sub>6</sub>, C<sub>6</sub>Rb<sub>2</sub>C<sub>6</sub>, and C<sub>6</sub>Cs<sub>2</sub>C<sub>6</sub> in BLG. Reproduced with permission,<sup>[71]</sup> 2024, Springer Nature.

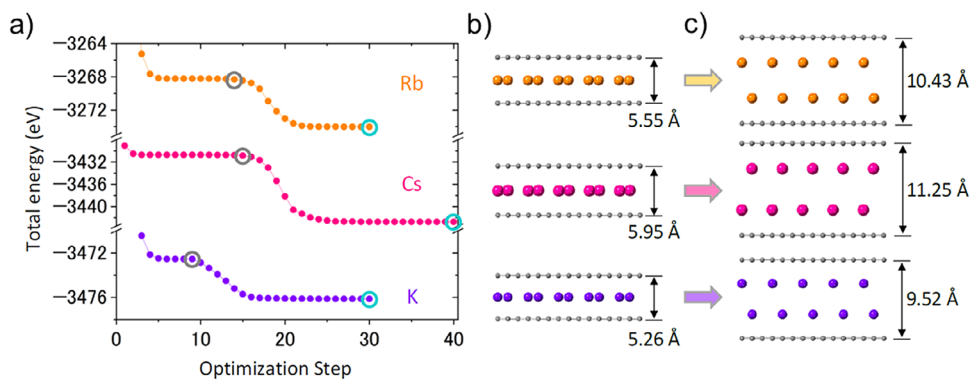


**Figure 7.** Geometry optimization for the C<sub>6</sub>K<sub>2</sub>C<sub>6</sub>, C<sub>6</sub>Rb<sub>2</sub>C<sub>6</sub>, and C<sub>6</sub>Cs<sub>2</sub>C<sub>6</sub>. a) The calculated total energy corresponding to the geometry optimization steps for K, Rb, and Cs intercalated in BLG. b,c) The atomic models corresponding to the first and second optimized plateau, marked by grey and cyan circles. The total energy is lower when the alkali metal layers are separated at different heights. Reproduced with permission [71], 2024, Springer Nature

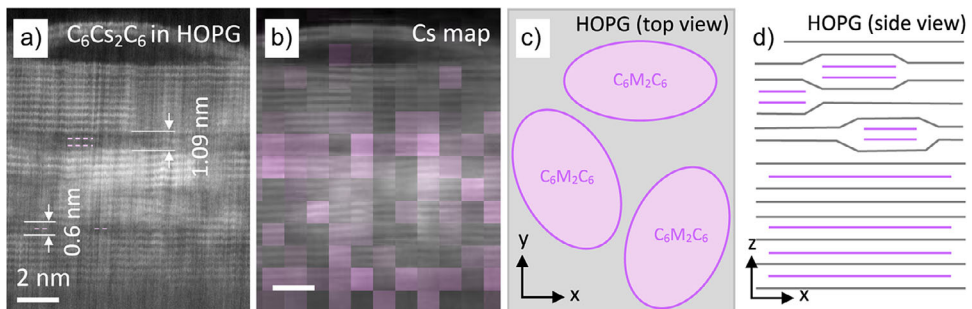


**Figure 8.** a) Cross-sectional ADF image of Cs intercalated HOPG (highly oriented pyrolytic graphite). Bilayer Cs is found near the surface layers, while single layer Cs is found in the deeper layers of graphite. b) Corresponding EELS (electron energy loss spectroscopy) Cs intensity mapping from the same area as in (a). c) Schematic illustration of the top view of the AM intercalation in HOPG, highlighting the  $C_6M_2C_6$  domains in pink. d) Schematic illustration of the side view of AM intercalation in HOPG, emphasizing the wrapping of the AM bilayer domain by the surface graphite layers and the single-layer AM intercalated in the deeper layer of graphite. Reproduced with permission.<sup>[71]</sup> 2024, Springer Nature.

than in graphite structures.<sup>[104]</sup> This makes  $MoS_2$  combined with conductive carbon matrices a particularly promising approach. For instance, *graphene/MoS<sub>2</sub>* heterostructures demonstrate high Li-intercalation capacitance (up to 1300 mAhg<sup>-1</sup>).<sup>[96]</sup> Numerous theoretical studies have explored AM intercalation in  $MoS_2$ /graphene systems, analyzing their stability, charge transfer mechanisms, and electronic structure in detail.<sup>[104–115]</sup>

However, all the presented experimental and theoretical works have focused on studies of single-layer AM intercalation in the *graphene/MoS<sub>2</sub>* heterostructure. Inspired by the works on multilayer AM structures in BLG,<sup>[27,28]</sup> the intercalation of Li, Na and K into the Gr/ $MoS_2$  bilayer heterostructure has been systematically studied by Chepkasov and Krasheninnikov<sup>[29]</sup> using first-principles calculations. To determine the most energetically favorable configurations of AM multilayers, different initial structures of AM atoms were considered. The initial atomic positions were cut from bulk *fcc*, *hcp*, and *bcc* metals along low-energy directions (e.g., [111] for *fcc* structures) and placed between graphene and  $MoS_2$  layers. The intercalation energies as a function of AM atom concentration for single and multilayer structures are shown in Figure 9b,e,g. In the case of Li such structures can be formed due to its negative intercalation energies. For Na it is interesting that the intercalation energy for *bcc* and *hcp* multilayers is negative with the same value as for a single layer with an atomic concentration higher than 0.6. These results indicate that the formation of Na multilayers in Gr/ $MoS_2$  is possible at high concentrations of Na atoms. The same results were obtained for K, but only for the *bcc* and *fcc* structures. As shown in previous theoretical<sup>[116–118]</sup> and experimental<sup>[119–121]</sup> studies a transition from the trigonal 2H-phase of  $MoS_2$  to the octahedral 1T-phase and then to the distorted 1T'-phase occurs with increasing Li concentration. The transition from the 2H-phase to the distorted 1T'-phase is associated with a significant energy barrier, which decreases significantly with increasing Li concentration. It is important to note that the 2H- $MoS_2$  layer is a semiconductor, whereas 1T'- $MoS_2$  possesses metallic conductivity. This phase transition is promoted by the charge transfer from the intercalated Li atoms to  $MoS_2$  layer. Transition from 2H to 1T' occurs when  $\approx 0.46$  e<sup>-</sup> flows to each Mo atom from the Li.<sup>[29]</sup> Only in the presence of Li multilayer structures (in the case of *bcc* and *hcp*) allows the required number of electrons to flow to  $MoS_2$  (Figure 9a). The intercalation energies of all Li structures located between Gr/2H-

MoS<sub>2</sub> and Gr/1T'-MoS<sub>2</sub> heterostructures were compared and it was found that in the case of *bcc* and *fcc* configurations the 1T' phase is energetically more favorable. These results indicate that a phase transition from 2H to 1T' should indeed occur in the  $MoS_2$  layer during the formation of Li multilayer structures. The Na and K multilayer structures do not give up enough electrons for the transition (Figure 9d,f), which is consistent with calculations of the total energies of the systems showing that the 2H phase has a lower energy.

### 3. Graphite with Atomic Channels

The pursuit of high-energy-density batteries has been hampered by the inherent limitations of conventional Li metal anodes, particularly uncontrolled dendrite growth and slow ion transport kinetics. A paradigm shift was inspired by the pioneering work of Kuhne et al.,<sup>[28]</sup> who demonstrated that confined, multilayer compact Li metal could stably exist between two graphene layers. This discovery challenged the traditional view of Li deposition and suggested the potential for bulk-like Li storage within a carbon matrix. Building directly upon this concept, Zhou et al.<sup>[68]</sup> proposed a revolutionary pathway for Li diffusion through the bulk of carbon material. They developed a “pre-tunneling” technique for graphite, strategically engineering the structure to create a network of atomic-scale channels. This process simultaneously generates voids to accommodate Li and introduces lithophilic sites that guide Li nucleation, resulting in a continuous web of both interlayer and intralayer diffusion pathways. This architected material, termed a Bulk Diffusion Lithium Conductor (BDLC), facilitates the rapid and uniform transport of ultradense Li. The mechanism represents a fundamental departure from the conventional surface diffusion/deposition model. By redirecting Li transport from the surface into the bulk atomic channels, the BDLC effectively circumvents the root cause of dendrite formation non-uniform surface deposition. This leads to significantly improved electrochemical kinetics, as ions traverse shorter, more direct pathways, while simultaneously enhancing safety by suppressing short-circuiting dendrites. Consequently, this bulk-diffusion-dominated mechanism offers a promising route to overcome the critical bottlenecks facing next-generation Li metal batteries.

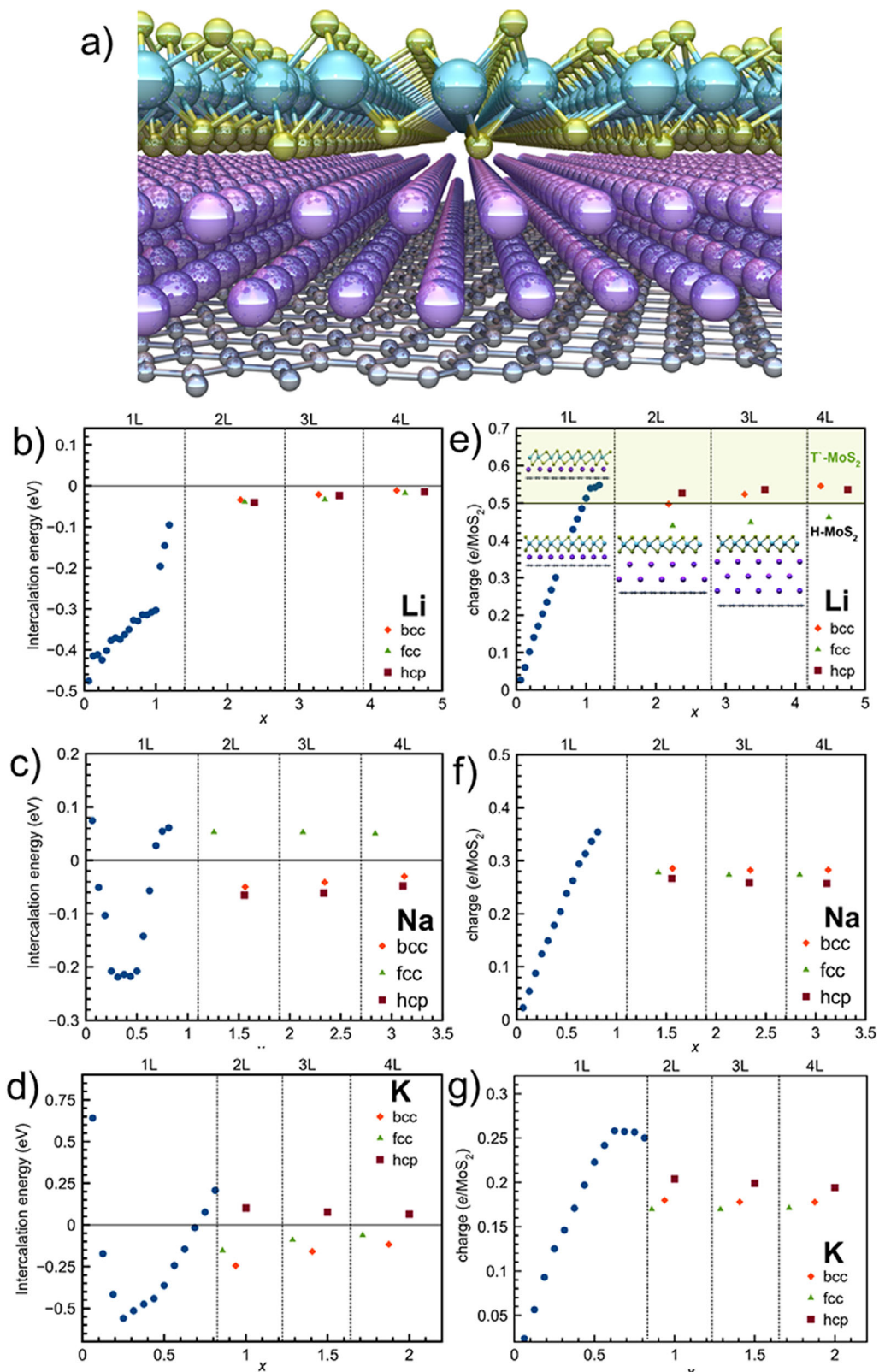


**Figure 9.** a) Typical atomic configurations illustrating the multi-layer structures of AMs between the sheets of the host material graphene and  $\text{MoS}_2$ . Intercalation energy as a function of the concentration of Li b), Na c), and K d) atoms in single-(1L), double-(2L), and multi-layer (3L and 4L) configurations in the Gr/ $\text{MoS}_2$  heterostructure. e–g) Corresponding charge transfers to  $\text{MoS}_2$  sheet in the heterostructure. Reproduced with permission,[29] 2022, American Chemical Society

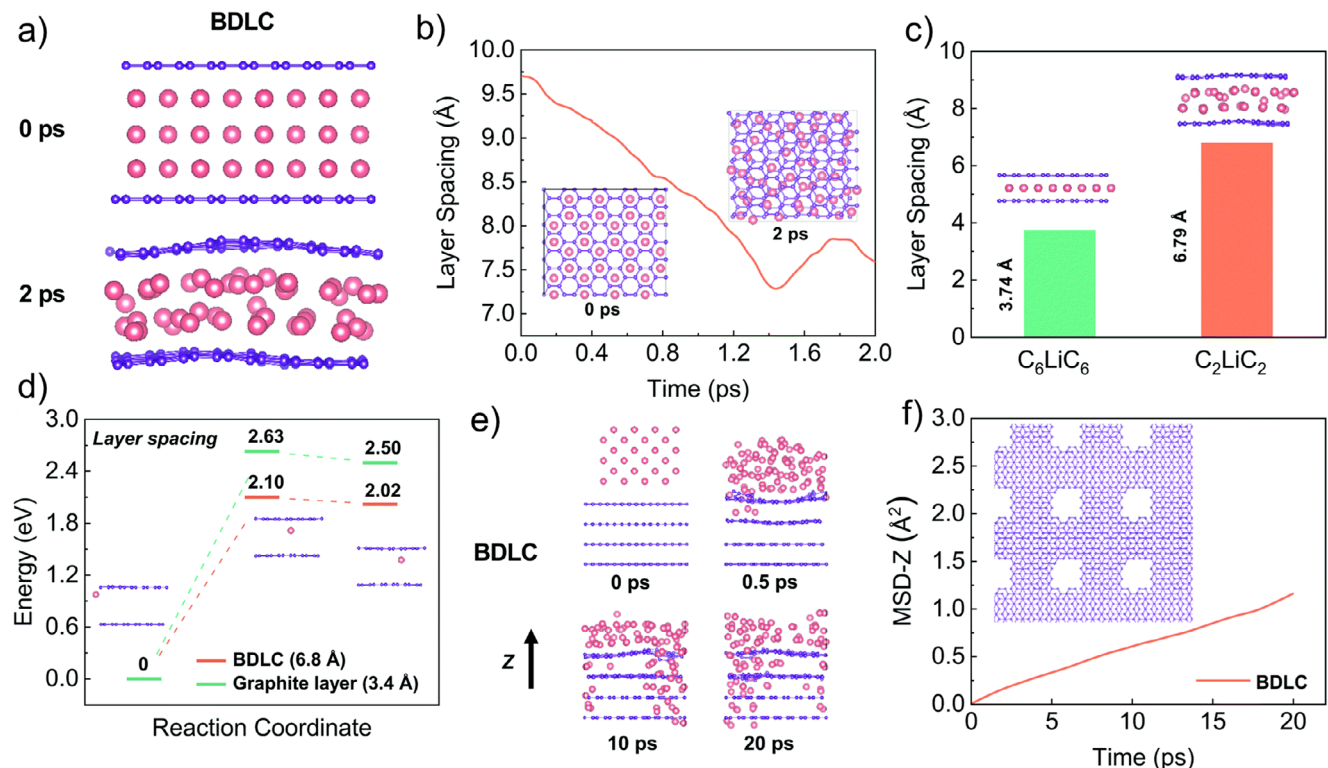


**Figure 10.** DFT calculations and AIMD simulations of Li diffusion through the atomic channels of BDLC (bulk diffusion Li conductor). a) Snapshots of AIMD simulations for interlayer diffusion in BDLC. b) Variation of layer spacing over time for interlayer diffusion according to AIMD simulations. The images in the inset of (b) correspond to the top view of snapshots. c) Layer spacing of  $C_6LiC_6$  and  $C_2LiC_2$ . The images in the inset of (c) correspond to the structure of  $C_6LiC_6$  and  $C_2LiC_2$ . d) Migration energy profiles of Li diffusion with respect to different layer spacings. The images in the inset of 2d are the structures of BDLC (6.8 Å) corresponding to the initial, transition and final state of Li diffusion. e) Snapshots of AIMD simulations for cross-layer Li diffusion in BDLC. f) MSD curves of Li diffusion along the z-axis direction. The images in the inset of (f) correspond to the top view of the typical model of BDLC for Li intralayer diffusion. The pink and violet balls represent Li and C atoms, respectively. Reproduced with permission.<sup>[68]</sup> 2022, Royal Society of Chemistry.

Previous DFT studies have primarily focused on the thermodynamic stability of superdense lithium within bilayer graphene, leaving the detailed atomistic mechanisms of its dynamic diffusion largely unexplored. To address this, Zhou et al.<sup>[68]</sup> conducted comprehensive ab initio molecular dynamics (AIMD) simulations at 300 K to probe the diffusion kinetics across different Li layer configurations. Their simulations reveal a structural evolution where, upon optimization, the Li redistributes and condenses into a denser state, ultimately stabilizing in a  $C_2LiC_2$  configuration (Figure 10a,b). This intercalation of triple the Li content compared to a standard  $C_6LiC_6$  structure necessitates a significant expansion of the graphene interlayer spacing from 3.74 to 6.79 Å confirming that an enlarged layer spacing is a critical prerequisite for ultra-dense Li storage and transport (Figure 10c).

To quantitatively evaluate the diffusion kinetics, the authors employed the climbing image nudged elastic band (CI-NEB) method, calculating the energy barrier for Li migration within the bulk diffusion Li conductor (BDLC) at varying interlayer spacings (3.4 to 6.8 Å). The results demonstrate that for an identical atomic arrangement, a larger interlayer distance correlates with a lower diffusion energy barrier and a more stable final state within the BDLC. This effect is further amplified by the presence of nitrogen active sites in the graphene lattice, which additionally reduce the energy barrier.

Crucially, AIMD simulations of cross-layer diffusion for high-density Li show that transport occurs predominantly through the pre-formed voids of the BDLC. This bulk diffusion mechanism is quantitatively validated by the time evolution of the mean square displacement along the z-axis (MSD-Z) (Figure 10e,f). Collectively, these findings provide compelling multi-faceted evidence that the atomic channels in the BDLC architecture enable the efficient and rapid diffusion of high-density Li.

To engineer atomic channels within graphitic carbon (GC), Zhou et al.<sup>[68]</sup> employed a molecular tunneling technique, penetrating standard graphite layers using thermally activated  $NH_3$  molecules. Upon heating,  $NH_3$  decomposes into reactive radicals (e.g.,  $NH_2$ , NH, H), which etch and diffuse into the graphite lattice. This process simultaneously creates two key features: expanded interlayer galleries and intralayer voids, effectively forming a network of diffusion channels.<sup>[122]</sup> This  $NH_3$ -based thermal treatment is notably scalable for large-volume production. Scalability is achieved through the design of precise mechanical components in the tube furnace and strict regulation of a uniform  $NH_3$  environment with controlled concentration and flow rate.

The structural outcome of this molecular tunneling is evident in high-resolution transmission electron microscopy (HRTEM) images. As shown in Figure 11d,e, the resulting material exhibits a distinct morphology characterized by tortuous layer stacking

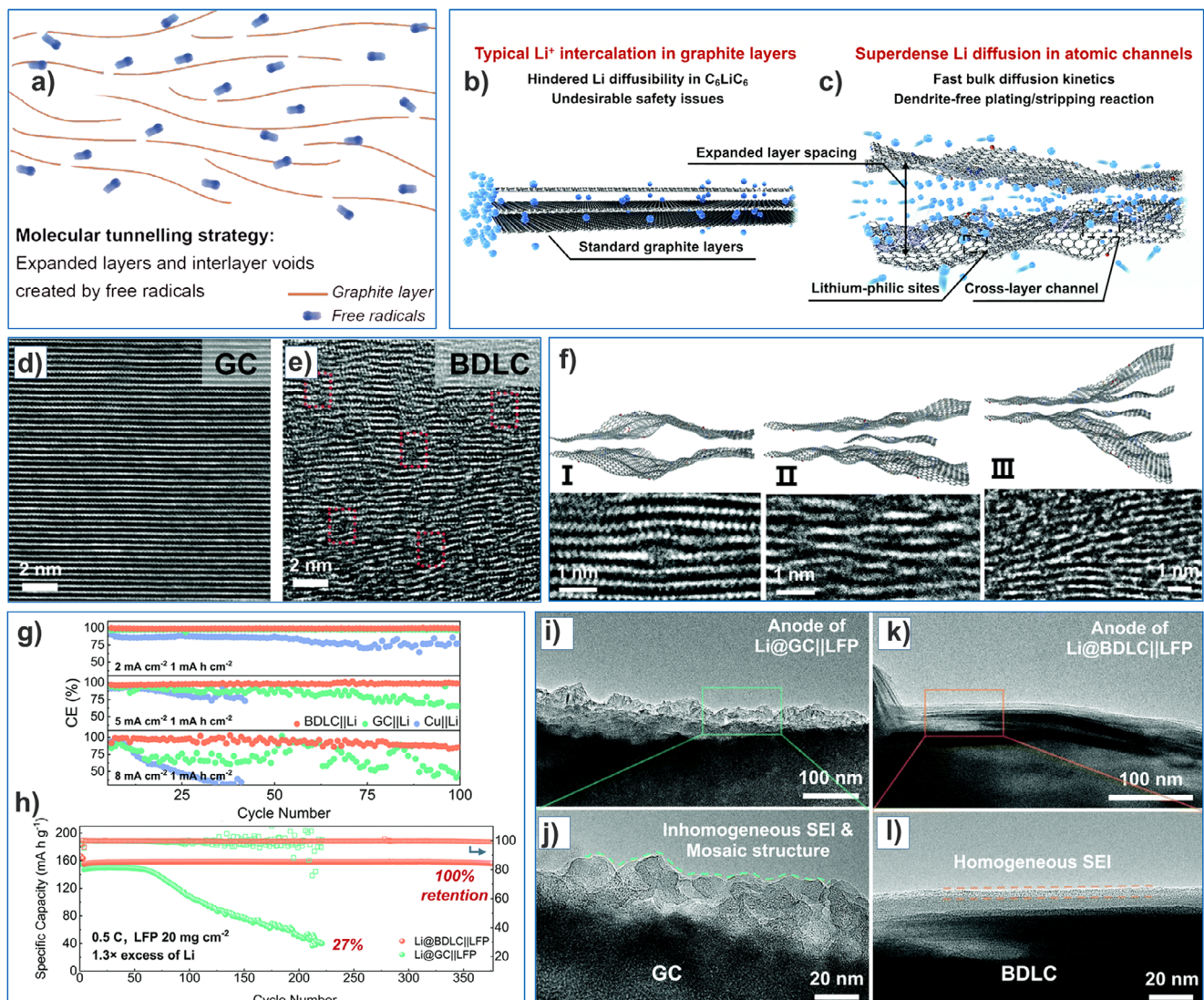


**Figure 11.** a) Schematic illustration of molecular tunnelling strategy. b,c) Comparative illustration of graphite layers and atomic channels. Schematic illustration of (b) typical  $\text{Li}^+$  intercalation in graphite layers and (c) superdense Li diffusion in atomic channels. Aberration corrected HRTEM images of the interlayer structure of d) GC and e) BDLC. The expanded layer spacings are marked with red squares. f) Schematic illustration along with the HRTEM images of a typical expanded interlayer structure of BDLC, including the (I) bulging channel, (II) single-layer-graphene supported channel and (III) multi-layer-graphene supported channel. g) CE at a current density of 2, 5 and 8  $\text{mA cm}^{-2}$  for 1  $\text{mAh cm}^{-2}$ . h) Comparison of cycling performance between Li@BDLC||LFP and Li@GC||LFP with high LFP areal loading of 20  $\text{mg cm}^{-2}$ , 1.3 x limited excess of Li, at 0.5 C. HRTEM images of cycled (i,j) Li@GC and (k,l) Li@BDLC and anodes at different magnifications. Reproduced with permission,<sup>[68]</sup> 2022, Royal Society of Chemistry.

and increased interlayer spacing. Crucially, this structural modification is achieved without sacrificing the long-range order of the graphite crystallites, preserving the essential conductive framework.

Three typical interlayer channels (I) bulging channel, (II) single-layer-graphene supported channel, and (III) multi-layer graphene-supported channel can be formed in BDLC (Figure 11f). The undulating interlayer structure and small graphene nanosheets stabilize the highly expanded graphite layers. The average interlayer spacing can vary by 170%, from 3.33 Å (GC) to 5.65 Å, and in some cases the interlayer spacing can reach  $\approx$ 7 Å. Heat treatment at 450 °C leads to the most optimized interlayer structure, avoiding under-expansion and

collapse of the structure. The intralayer structure of BDLC also undergoes obvious changes with the formation of abundant interlayer voids.

After the formation of atomic channels, BDLC was validated in a real coin-type cell.<sup>[68]</sup> To compare GC and BDLC ex situ SEM characterization is performed to observe the plated/stripped Li morphologies at the 1<sup>st</sup>, 5<sup>th</sup> and 10<sup>th</sup> cycles (0.5  $\text{mA cm}^{-2}$ , 5  $\text{mAh cm}^{-2}$ , ester-based electrolyte). Experiments<sup>[68]</sup> have shown that BDLC exhibits a uniform and stable Li plating/stripping reaction after several cycles, in contrast to GC where the Coulombic efficiency (CE) decreases to 65.8% after 10 cycles (with 96.6% for BDLC) with the formation of filamentous Li dendrites, which can lead to battery failure and safety issues.<sup>[123,124]</sup> The study of

the Li plating/stripping reversibility of BDLC and GC showed that at current densities of 2 and 5 mA cm<sup>-2</sup>, with an areal capacity of 1 mAh cm<sup>-2</sup>, BDLC||Li delivers a stable CE with increasing current densities, maintaining 99.6 and 98.6% after 100 cycles, respectively. Even at a fast-charging current density of 8 mA cm<sup>-2</sup>, BDLC||Li can still operate stably after 100 cycles (85.9%), while GC||Li would experience an obvious fluctuation of CE and decrease rapidly (Figure 11g). Due to the presence of atomic channels, Li in BDLC achieves fast diffusion and the decrease in cycling caused by the growth of Li dendrite is effectively suppressed. To investigate the potential of BDLC application, full cells were assembled by pairing Li@BDLC anodes with LFP cathodes. Compared to Li@GC||LFP, which retains only 27% of the initial capacity after 220 cycles, Li@BDLC||LFP achieves ultrahigh cycle stability and retains 100% capacity for 370 cycles (Figure 11h). In order to understand the reasons for the distinct difference in electrochemical characteristics, an ex situ TEM investigation of Li@BDLC||LFP and Li@GC||LFP was carried out after rate performance at a discharge state.<sup>[68]</sup> Li@BDLC and Li@GC anodes show a distinct difference on the surface, in particular, compared to the homogeneous surface structure of Li@BDLC (Figure 11k,l), Li@GC has a thick and rough surface (Figure 11i). Higher magnification examination reveals the irregular mosaic and heterogeneous structure of the solid electrolyte interphase (SEI) layer of Li@GC (Figure 11j). Thus the atomic BDLC channels promote uniform Li deposition/removal at different rates, reduce targeted surface Li nucleation and enable dendrite-free electrochemical performance. Thus, Zhou et al.<sup>[68]</sup> proposed for the first time the molecular tunneling strategy to construct atomic channels in graphitic bulk to enable fast diffusion of superdense Li without dendrite formation. A real coin-type cell based on BDLC demonstrates the highest areal capacity of 3.9 mAh cm<sup>-2</sup> and 100% capacity retention for 370 cycles. Zhou et al.<sup>[68]</sup> demonstrated the possibility of bulk diffusion through atomic channels, which is a new way to control reversible Li plating/stripping for dendrite-free Li metal batteries.

#### 4. Hard Carbon

Within the carbon anode family, hard carbon (HC) has emerged as a leading alternative to graphite, attracting considerable scientific interest due to its unique structural properties and promising electrochemical performance for alkali metal-ion batteries.<sup>[66,125–127]</sup> A significant advantage of HC lies in its sustainable production, it can be derived from a wide variety of low-cost, abundant biomass precursors such as wood, peat moss, lignin, and banana leaves, offering a pathway to environmentally and economically viable energy storage.<sup>[128,129]</sup> The formation of HC is intrinsically linked to the precursor's molecular structure. Precursors rich in sp<sup>2</sup>-hybridized carbon, such as aromatic petroleum derivatives, tend to form soft, graphitizable carbon, while those with high sp<sup>3</sup>-hybridized carbon content, like cellulose and plastics, typically yield the disordered, non-graphitizing structure characteristic of hard carbon.<sup>[129]</sup>

This non-graphitizing nature results in a highly complex and disordered architecture, a stark contrast to the nearly perfect, ordered layers of graphite. The high mechanical hardness of HC prevents the flattening and ordered stacking of graphene sheets during high-temperature treatment.<sup>[125]</sup> Consequently,

the HC structure is a complex mixture of short, curved, and entangled graphene domains interspersed with fullerene-like nanostructures.<sup>[125,130,131]</sup> These highly defective graphene sheets contain numerous vacancies, heteroatomic impurities, and non-hexagonal carbon rings (e.g., penta- and heptagons) that facilitate sheet curvature.<sup>[130,132,133]</sup> The sheets stack to a limited extent, typically forming small domains of two to five layers with an expanded interlayer spacing of 3.7–4.0 Å, and create a distribution of nanopores of varying sizes.<sup>[131,134,135]</sup>

This intricate molecular-level architecture, which can be tuned during synthesis via parameters like annealing temperature to adjust electrochemical performance,<sup>[134,136]</sup> gives rise to two fundamental and defining characteristics of HC. First, the presence of diverse structural features expanded interlayers, nanopores, and defects creates multiple, distinct types of sites for the reversible accommodation of alkali metal ions. Second, unlike the well-defined staging mechanism and capacity limit of graphite, the capacity of HC remains elusive and highly dependent on its specific nanostructure. A comprehensive understanding of these two issues the nature of the active sites and the origin of capacity is essential to rationally guide the development of high-performance HC anode materials.

#### 4.1. Li, Na Inside Hard Carbon

The growing demand for large-scale energy storage, particularly for renewable energy integration and grid stabilization, has highlighted the limitations of lithium-ion batteries (LIBs), primarily due to the high cost and uneven global distribution of lithium resources.<sup>[137,138]</sup> In this context, sodium-ion batteries (NIBs) have emerged as a compelling alternative, leveraging the natural abundance, low cost, and wide availability of sodium and its electrolyte salts.<sup>[139–142]</sup> However, a significant challenge in developing NIBs has been the anode material, as graphite the cornerstone of LIB anodes exhibits negligible capacity for sodium ion storage due to an unfavorable thermodynamic equilibrium with its ordered layered structure.<sup>[87,88,143]</sup>

Hard carbon has consequently risen as the most promising anode candidate for NIBs, with its unique structural features directly addressing the shortcomings of graphite. The disordered, turbostratic structure of HC, comprising expanded interlayer spacing, nanopores, and defects, provides ample active sites for the reversible insertion and storage of sodium ions.<sup>[66,125,126,144,145]</sup> This enables stable long-term cycling and delivers a high reversible specific capacity, often exceeding 300 mAh g<sup>-1</sup>, making HC an ideal and effective anode material for commercially viable sodium-ion batteries.

The storage mechanisms of lithium, sodium, and potassium in hard carbon remain a subject of intense debate, largely due to the material's complex and heterogeneous microstructure, which comprises numerous discrete morphological features.<sup>[146,147]</sup> A comprehensive comparative study by Kim et al.<sup>[148]</sup> highlighted fundamental differences in how hard carbon stores these alkali ions. For lithium, a sloping voltage profile is attributed to intercalation into the graphitic lattices of hard carbon. In contrast, sodium storage is dominated by adsorption onto the inner surfaces of closed pores, with the plateau capacity being directly governed by the total volume of these pores.

Understanding these distinct mechanisms necessitates a clear picture of the hard carbon microstructure. The evolution of these structural models began with Franklin's pioneering work,<sup>[149]</sup> which graphically depicted solid carbon as randomly oriented graphitic nanodomains surrounded by amorphous regions. This was later supported by Ban et al.,<sup>[150]</sup> whose TEM studies revealed curved graphite flakes forming a banded structure around pores in non-graphitizing carbons. As characterization techniques advanced, more sophisticated 3D models emerged, drawing analogies to fullerene-like structures and revealing a high concentration of defects, vacancies, and heteroatoms within the graphene-like flakes.<sup>[125,151]</sup>

To reconcile this complexity with electrochemical behavior, Chu et al.<sup>[152]</sup> recently proposed a revised structural framework, categorizing the hard carbon microstructure into three primary components: crystallites, defects, and nanopores. This tripartite model provides a valuable lens through which to analyze storage mechanisms. Consequently, the rational design of an ideal hard carbon anode requires precise control over these microcrystalline parameters. Achieving this goal will depend on combining advanced characterization techniques with theoretical calculations to unequivocally reveal the structure-property relationships governing alkali metal atom storage efficiency.

#### 4.2. Storage Mechanism of Hard Carbon

Hard carbon is the leading anode candidate for sodium-ion batteries. Its sodium storage behavior, typically characterized by a sloping and a plateau region in the discharge profile, remains a subject of intense debate. To explain this profile, several mechanisms have been proposed, which can be broadly categorized into three processes: capacitive adsorption on surfaces, sodium insertion into carbon interlayers, and nanopore filling. Specific models that combine these processes include the "insertion-adsorption" mechanism, the "adsorption-insertion" mechanism, the "adsorption-insertion-nanopore filling" mechanism, and the "adsorption-nanopore filling" mechanism (see Figure 12a-d).

The first model for sodium storage in hard carbon, the "insertion-adsorption" mechanism, was proposed by Stevens and Dahn in 2000.<sup>[153]</sup> They analogized the hard carbon structure to a stack of playing cards, featuring a mix of parallel layers and disordered regions with intervening nanopores (Figure 12a). In this model, the sloping region of the discharge curve corresponds to sodium insertion between the carbon layers, while the plateau region is attributed to sodium adsorption within the nanopores. Although subsequent studies using ex situ XRD and SAXS techniques provided confirmation for this mechanism,<sup>[151,154]</sup> it was later established that not all hard carbons conform to this "insertion-adsorption" model.<sup>[155]</sup>

In 2012, an alternative "adsorption-insertion" mechanism was proposed, attributing the sloping region to sodium adsorption on surface defects and the plateau to insertion into graphitic domains.<sup>[156]</sup> This model was later substantiated when the intercalation behavior during the plateau region was directly confirmed.<sup>[157]</sup> However, factors such as heteroatom doping can hinder this mechanism.<sup>[154]</sup> A key piece of evidence is the strong correlation between defect concentration and slope capacity, a link solidified by Lu et al.,<sup>[158]</sup> who validated the "adsorption-

intercalation" model using electrochemical data, Raman spectroscopy, and XPS.<sup>[158]</sup>

Building on earlier models, Bommier et al.<sup>[159]</sup> proposed a three-step "adsorption-intercalation-filling" mechanism in 2015. Their analysis using the galvanostatic intermittent titration technique revealed a distinct increase in the sodium diffusion coefficient at the end of the plateau region, which they interpreted as evidence of nanopore filling.<sup>[159]</sup> Subsequently, the "adsorption-filling" model was advanced and experimentally validated by Bai et al.,<sup>[160]</sup> Bin et al.<sup>[161]</sup> and Li et al.,<sup>[162]</sup> who found it to be a more accurate description for certain hard carbon structures. Further refining the mechanistic picture, Reddy et al.<sup>[163]</sup> recently proposed a detailed four-stage process: 1) adsorption on active surface sites, 2) insertion into interlayer defects, 3) layer filling, and finally, 4) sinking into nanopores.

The ongoing controversy stems from the fact that different hard carbons, derived from various precursors, exhibit distinct structural hierarchies that favor one mechanism over another. The structural evolution during carbonization is intrinsically linked to the molecular structure of the precursor, which directly dictates the resulting defect density, interlayer spacing, and pore size distribution.<sup>[164–166]</sup> Precursors such as sucrose, lignin, or cellulose typically yield hard carbons with a highly complex and heterogeneous architecture. They often inherit a significant volume of randomly distributed closed pores from the natural biomass template. These materials frequently exhibit a strong correlation between the plateau capacity and the total closed pore volume, lending strong support to the pore-filling mechanism as the dominant process in the low-voltage plateau.<sup>[167]</sup> Furthermore, the inherent presence of heteroatoms (e.g., O, N) in biomass can create numerous active defect sites, which significantly contribute to the sloping capacity via adsorption.<sup>[168]</sup> Synthetic precursors like polyvinylidene chloride (PVDC) or phenolic resins can lead to more tunable and homogeneous structures.<sup>[169]</sup> These carbons often show a clearer progression from adsorption to intercalation and finally to pore filling. For instance, hard carbons derived from PVDC have been shown to possess a well-defined "fullerene-like" microstructure with a high concentration of closed pores, making the "adsorption-filling" model particularly relevant.<sup>[170]</sup>

A contemporary understanding of sodium storage in hard carbon posits that multiple mechanisms operate concurrently, with their predominance dictated by the material's specific microstructure. This integrated view was significantly advanced by Au et al.,<sup>[171]</sup> who proposed that Na ion intercalation and adsorption occur simultaneously in the sloping region, while the low-voltage plateau is dominated by nanopore filling a model later confirmed by Weaving et al.<sup>[172]</sup> Adding atomistic detail, Surta et al. demonstrated that the sloping region involves a continuous evolution of Na ion binding sites, from six-member rings on flat graphene sheets to curved structures with odd-membered rings and fold sites.<sup>[173]</sup> The interplay within the plateau region is particularly nuanced. Chen et al. suggested that nanopore filling and intercalation can occur simultaneously, with their ratio highly dependent on the hard carbon's microstructure.<sup>[174]</sup> For stable pore filling to proceed, a suitable closed pore radius (with an optimal range of 1–2 nm) and sufficient internal defects to act as nucleation sites are critical.<sup>[175,176]</sup> Furthermore, a fully filled pore is energetically more favorable than a partially filled one.<sup>[177,178]</sup>

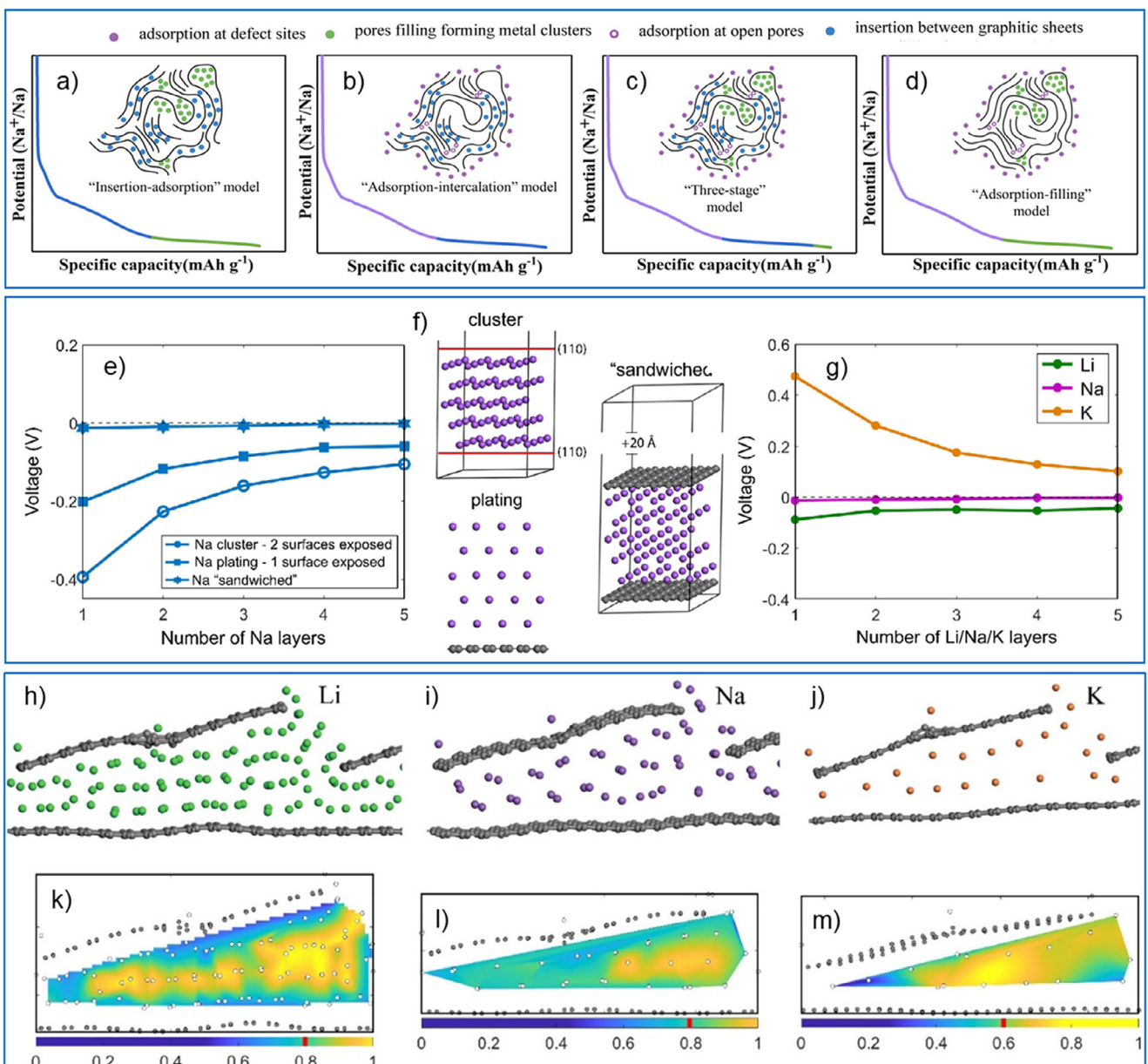


**Figure 12.** a-d) Schematic illustration of four mechanisms of sodium storage in hard carbons: a) insertion-adsorption model, b) adsorption-intercalation model, c) three-stage model, d) adsorption-filling model. Reproduced with permission,[235] 2022, John Wiley & Sons Inc. e) Voltage profile of one to five Na layers in cluster, plated, and sandwiched configurations. f) Depiction of the cluster, plating, and sandwiched configurations. g) Voltage profile of sandwiched Li, Na, and K layers. h-j) Li, Na, and K configurations of the completely filled pore. k-m) Cross section of the pore's electronic status for the completely filled configuration. Values close to 1 indicate metallic behavior as the valence charge resides with the alkali atom. Values close to 0 indicate ionic behavior as the valence charge is donated to the carbon matrix. The red stripe in the color bar specifies the average value. Note the different color scaling for K. Reproduced with permission,[181] 2022, American Chemical Society.

Computational studies provide fundamental support for this mechanism. DFT calculations indicate that Na atoms preferentially aggregate into small, triangular clusters on graphene sheets, indirectly supporting the clustering hypothesis within nanopores.<sup>[179]</sup> Moreover, DFT directly predicts that it is energetically favorable to form three to four quasi-metallic Na layers inside graphitic interlayers, confirming that the formation of such semi-metallic clusters is the origin of the low-voltage plateau.<sup>[176,180]</sup>

The mechanism of sodium storage in hard carbon remains contentious, primarily due to the material's complex and heterogeneous structure, which offers a wide variety of potential storage sites, from surfaces and defects to pores and graphitic interlayers. This structural complexity complicates the interpretation of the characteristic voltage profile and has led to conflicting conclusions across experimental and computational studies. To resolve these controversies and provide a fundamental understanding of how alkali metals interact with specific carbon defects, detailed

theoretical work is required. The following section discusses such a comprehensive study by Vasileiadis et al.,<sup>[181]</sup> which addresses these very challenges.

#### 4.3. Theoretical Calculations of Alkali Metals Inside Hard Carbon

Vasileiadis et al. employed density functional theory to provide a detailed atomistic perspective on the interaction of alkali metals (Li, Na, K) with structural defects in hard carbon.<sup>[181]</sup> Their findings indicate that vacancy sites and edges serve as crucial binding centers, contributing directly to the capacity in the sloping voltage region. These sites also act as favorable nucleation points for metal clustering, although the formation of extended metallic islands necessitates a highly defective environment, going beyond isolated defects.

To elucidate the pore-filling mechanism responsible for the low-voltage plateau, the authors simulated three distinct sodium configurations: clusters, plates, and intercalated sandwich structures (Figure 12e,f). A key insight from this analysis is the significant energy penalty associated with the exposed (110) surfaces of metallic sodium, which drastically reduces the cell voltage. This penalty is mitigated when these surfaces contact pristine graphene, as the carbon matrix replaces the high surface energy with a more stable interfacial energy, thereby enhancing the overall thermodynamic stability of the system. This driving force leads sodium clusters to minimize their exposed surface area by becoming fully encapsulated by carbon sheets, explaining the thermodynamic preference for fully, rather than partially, filled pores. The voltage for this stabilized, confined sodium is predicted to be close to 0 V.

Extending the analysis across alkali metals revealed distinct trends (Figure 12g). While lithium sandwich configurations follow a similar trend to sodium but with slightly lower voltages, potassium exhibits positive, gradually decreasing voltages. This is attributed to the highly favorable surface adsorption of K on graphene, which makes monolayer sandwiches more stable than multilayers. The relative electrochemical behavior of Li, Na, and K is governed by a balance between two competing factors: the energy penalty of the metal's (110) surface, which increases in the order  $E_K < E_{Na} < E_{Li}$ , and the stability gained from the metal-carbon contact, which favors the metals in the same sequence. This interplay successfully explains the observed voltage trends.

To elucidate the pore-filling process in hard carbon, Vasileiadis et al. employed a wedge-pore superstructure model that incorporated key structural features such as edge surfaces, vacancy defects, and pores of defined dimensions ( $3.70 \times 0.74$  nm) with a variable interlayer spacing (0.56 to 1.14 nm).<sup>[181]</sup> Their simulations revealed that lithiation, sodiation, and potassiation all initiate at the edge surfaces. The pore-filling mechanism proceeds sequentially; to minimize the energy penalty associated with exposed metal surfaces, it is energetically favorable to completely fill one pore before beginning to fill the next. This sequential filling results in a constant change in free energy, which manifests electrochemically as a transition from a sloping voltage profile to a distinct plateau.

As the alkali metal concentration on the edges increases, adsorption at defect sites (vacancies) becomes competitive and

eventually takes over as the dominant, energetically favorable process at higher concentrations. Analysis of the optimized filled pore configurations (Figure 12h–j) revealed average interatomic distances of 2.84 Å for Li–Li, 3.57 Å for Na–Na, and 4.76 Å for K–K. Bader charge analysis indicated a semi-metallic state for Li and Na within the pores, with an average of 20% electron transfer from the metal to the carbon matrix. Lithium atoms in direct contact with the carbon walls exhibited slightly higher electron transfer than sodium. In contrast, potassium donated ≈40% of its valence charge to the carbon. These computational findings for sodium, particularly the semi-metallic clustering and the degree of electron transfer, are in excellent agreement with experimental NMR studies<sup>[179,180]</sup> and other machine-learning DFT calculations.<sup>[182]</sup>

#### 4.4. Fast Charging in Hard Carbon Anodes

Recent advances have demonstrated the potential of structurally tuned hard carbons with low reaction strain for high-performance batteries. For instance, in LIBs, such hard carbon anodes have enabled impressive performance, achieving 82% capacity retention at a 6C rate over 500 cycles in pouch cells.<sup>[183]</sup> Similarly, hard carbon has shown promise as a fast-charging anode for sodium-ion batteries. A study by Rudola et al. demonstrated fast charging in a small pouch cell; however, this was achieved with limited areal capacity ( $\approx 1.3$  mAh cm<sup>-2</sup>) and a cycle life of only  $\approx 100$  cycles.<sup>[184]</sup> These results underscore a significant challenge: achieving long service life at high charging rates and high areal capacities remains difficult.

The practical application of hard carbon in high-power, large-format batteries is further complicated by the coexistence of sloping and plateau regions in its voltage profile. This characteristic complicates state-of-charge estimation and power management. Moreover, elucidating the fundamental relationship between the complex carbon microstructure, the dominant sodium storage mechanism, and the resulting fast-charging performance constitutes a critical yet formidable task for the field.

To elucidate the structural features of hard carbon (HC) that govern fast-charging performance, Li et al. conducted a comprehensive quantitative study, integrating theoretical modeling with experimental validation of the lithiation/sodiation processes.<sup>[185]</sup> Their work separately analyzed the contributions of the sloping and plateau regions, which are typically attributed to distinct mechanisms: the slope is commonly associated with adsorption or intercalation, while the plateau is linked to pore filling, as established in prior research.<sup>[186,187]</sup>

A wedge-pore model featuring edges, vacancies and pore structures, Li et al.<sup>[185]</sup> were constructed to replicate the typical microstructure of HC. They simulated the electrochemical process by populating this model with Li and Na atoms in energetically competing configurations, followed by geometry and energy optimization. The resulting simulated voltage profiles for Li and Na are shown in Figure 13a. The simulations confirm that sodiation/lithiation initiates at defect sites (edges and vacancies), generating the sloping voltage region. The process then progresses to a pore-filling stage, where each graphene sheet on the inner pore surface accommodates one to two layers of alkali metal atoms (Figure 13a).

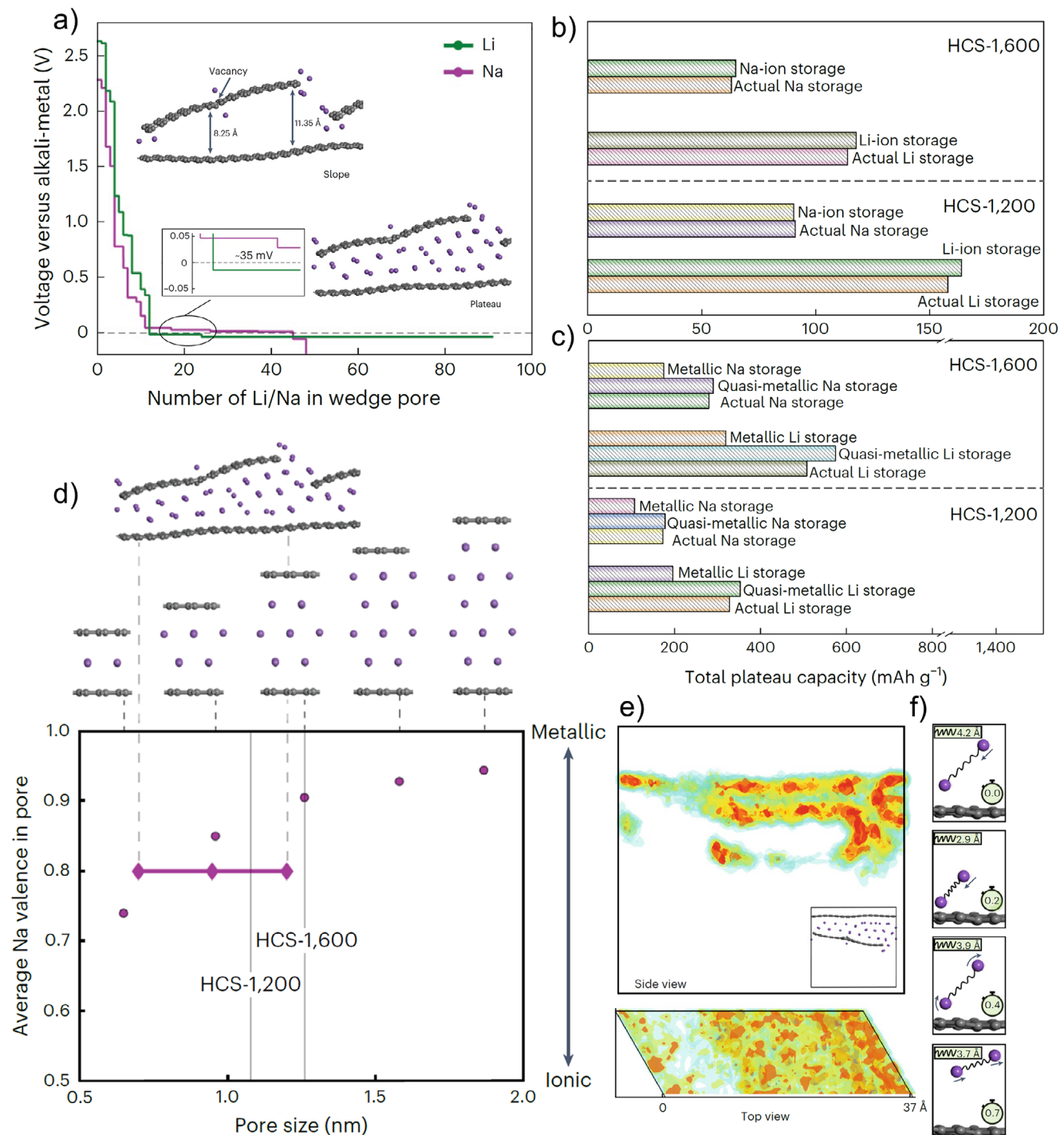


**Figure 13.** a) DFT calculated voltage profiles of the wedge-pore lithiation and sodiation. b) Comparison between the experimental sloping capacities and calculated sloping capacities of HCSs for Li and Na storage. c) Comparison between the experiment plateau capacities and calculated plateau capacities based on simulative processes of Li or Na storage in the wedge-pore model. d) Average Na valence charge for the wedge pore is plotted as well in comparison with the average experimental pore size of HCS-1200 and HCS-1600. e) Na density plot over the 18 ps MD simulation at 600 K depicted from the side and top view. The Na density is interconnected, covering the whole pore region, revealing that Na can quickly diffuse, being able to access all parts of the nanopore within small time frames. f) Depiction of correlated diffusion in the pore. The spring subplot refers to the Na–Na distances in Å, and the timer counts in ps. Reproduced with permission.<sup>[185]</sup> 2024, Springer Nature.

Furthermore, the study provided direct evidence linking the plateau capacity to the volume of closed pores. By demonstrating a strong correlation between the calculated pore-specific capacity and experimental data, Li et al. conclusively confirmed that pore filling is the mechanism responsible for the high-capacity voltage plateau (Figure 13c).

Both experimental and theoretical analyses reveal a fundamental difference in the voltage profiles of lithium and sodium in hard carbon anodes. A key distinction is the potential of the plateau region: sodium resides at a slightly positive voltage ( $\approx 35$  mV), whereas lithium plateaus at a negative potential (Figure 13a). This critical difference explains the absence of a distinct Li plateau without over-discharge. The underlying mechanism, as elucidated by Vasileiadis et al.,<sup>[181]</sup> involves the stabilization of alkali metal surfaces by graphene interfaces. When Li or Na surfaces contact carbon walls, the high energy penalty of the exposed metal surface is reduced, thereby increasing the cell voltage. This stabilizing effect is more pronounced for Na than for Li, resulting in a higher plateau potential for sodium. Consequently, the system thermodynamically favors the formation of completely filled pores, where the carbon matrix fully “wets” the metal surfaces to eliminate energy penalties.

This voltage characteristic has significant practical implications. The positive sodium plateau enhances resilience against polarization, mitigating the risk of sodium metal plating during fast charging and thus improving safety.<sup>[188]</sup> For complete pore filling to occur efficiently, pore size is critical. Excessively large pores permit extensive metal nucleation, re-introducing a significant surface energy penalty. This can drive the voltage to the lower cutoff limit before stable carbon-metal interfaces can be established, preventing the pore-filling mechanism from stabilizing the system and leading to capacity loss.

The interplay between nucleation and surface coverage points to the existence of an optimal pore size, which theoretical and experimental studies have consistently placed at  $\approx 1$  nm.<sup>[136]</sup> DFT calculations indicate that a pore of this dimension can accommodate 2-3 layers of sodium or 3-4 layers of lithium.<sup>[185]</sup> Pores larger than this optimal size are detrimental, as they induce a higher degree of metallic character in the alkali metal clusters, which in turn slows the (dis)charging kinetics. This relationship between pore size and the average valence charge of the metal is illustrated in Figure 13d.

The practical significance of this size constraint is confirmed by experimental work on hard carbon spheres (HCS). A comparison between HCS synthesized at 1200 and 1600 °C revealed that the smaller average pore size in HCS-1200 ( $\approx 1.08$  nm versus  $\approx 1.26$  nm in HCS-1600) directly contributed to its superior fast-charging performance.<sup>[182]</sup> This finding underscores that an effective strategy for achieving high capacity and rapid storage is to maximize the population of relatively small pores within the hard carbon structure.

Further insight into the fast-charging capability comes from ab initio molecular dynamics simulations.<sup>[185]</sup> These studies reveal that sodium atoms within a pore are highly mobile on short timescales ( $\approx 18$  ps). Although sodium tends to cluster, it can diffuse rapidly within the pore in a liquid-like manner. Notably, the simulations observed correlated motion, where two sodium atoms form a dipole and migrate together in a single, coordinated jump within 1–3 ps (Figure 13e). This phenomenon of pair-

wise migration, expected in the absence of screening between atoms, is a known mechanism that facilitates exceptionally fast ion diffusion.<sup>[28,189]</sup>

By studying in detail all the factors that affect the charging rate of hard carbon Li et al.<sup>[185]</sup> succeeded in creating a fast charging hard carbon based battery. Based on the HCS-1200 it was possible to create a full Na-ion cell that retains 83% of its capacity after 3000 cycles at a cycle rate of 6.5 C. Large NIBs using the layered  $\text{Na}(\text{Cu}_{1/9}\text{Ni}_{2/9}\text{Fe}_{1/3}\text{Mn}_{1/3})\text{O}_2$  cathode and anode HCS-1200 provide  $\approx 3$  Ah at 0.1 C and boosts a high areal capacity of  $\approx 2.2$  mAh cm $^{-2}$ . This cell showed one of the shortest charge times ( $\approx 9$  min) and one of the longest cycle lives ( $\approx 3000$  cycles) at the high charge rate with the highest mass loading of active materials ( $7\text{--}8$  mg cm $^{-2}$ ).

## 5. Soft Carbon

The pursuit of higher energy density in lithium batteries has driven significant interest in replacing graphite anodes with metallic lithium. Lithium metal offers an unparalleled theoretical capacity of 3860 mAhg $^{-1}$  (2064 mAhcm $^{-3}$ ) and the lowest electrochemical potential, establishing it as the ultimate anode material.<sup>[177,190,191]</sup> However, its commercialization is impeded by critical challenges related to safety and cyclability. These issues primarily stem from the growth of lithium dendrites during cycling and low Coulombic efficiency.<sup>[192]</sup>

The dendritic morphology not only accelerates capacity fade by consuming active lithium and electrolyte but also poses a severe safety risk, as dendrites can penetrate the separator, cause internal short circuits, and lead to thermal runaway.<sup>[193]</sup> The propensity for dendrite formation is rooted in the intrinsic properties of lithium, including its low surface energy and high atomic mobility, which favor 1D whisker growth.<sup>[194]</sup> Furthermore, in solid-state battery configurations, the problem is exacerbated by interfacial instability. As demonstrated by Kasemchainan et al.,<sup>[195]</sup> lithium metal tends to form voids within solid-state electrolytes during stripping, leading to poor interfacial contact, elevated resistance, and uneven current distribution. This, in turn, promotes localized lithium plating and dendrite nucleation during subsequent charging cycles.

To mitigate interfacial instability in all-solid-state lithium-metal batteries (ASSLMBs), researchers have engineered various protective interlayers, including ZnO, LiF, and graphite, among others.<sup>[196–198]</sup> Despite these efforts, the achievable current density and areal capacity of ASSLMBs remain insufficient for commercial viability. A fundamental challenge lies in the dendrite formation mechanism, which is governed by the competition between the rate of Li $^{+}$  reduction and the rate of ionic replenishment at the electrode interface. At high current densities, the accelerated reduction of Li $^{+}$  to Li increases the likelihood of dendrite nucleation. If the ionic flux cannot keep pace, localized space charge accumulates, promoting dendritic growth.<sup>[199,200]</sup>

This problem is exacerbated in solid-state systems because Li $^{+}$  deposition is confined strictly to the anode/SSE interface. The low diffusion coefficient of Li $^{+}$  within the anode bulk prevents inward transport, forcing all reduction reactions to occur two-dimensionally at the interface. This leads to deleterious local current densities, mechanical stress, and volume changes that rapidly initiate dendrites.<sup>[201,202]</sup>

A promising solution involves designing protective layers with high  $\text{Li}^+$  diffusion coefficients and multidimensional transport pathways to guide lithium deposition in a 3D manner. This 3D deposition mode homogeneously distributes the electric field, reduces the local current density, and mitigates ionic depletion, thereby effectively increasing the critical current density, suppressing dendrites, and enhancing rate capability.<sup>[70]</sup>

To address the persistent challenge of dendrite growth and enhance the cycle life of all-solid-state lithium-metal batteries (ASSLMBs), Wang et al. proposed an innovative anode design using modified soft carbon.<sup>[70]</sup> Soft carbon possesses a naturally larger interlayer spacing than graphite, which is beneficial for ion transport. The key innovation lies in a calcination process using thiourea, which decomposes to generate ammonia ( $\text{NH}_3$ ) and hydrogen sulfide ( $\text{H}_2\text{S}$ ) in situ. The hot  $\text{NH}_3$  molecules, with a kinetic diameter slightly larger than the pristine interlayer distance, act as a “molecular tunnel” to further expand the carbon galleries, thereby facilitating  $\text{Li}^+$  diffusion. Concurrently,  $\text{H}_2\text{S}$  and  $\text{NH}_3$  gases etch the carbon framework, introducing disorder and creating covalent C–S and C–N bonds through doping.

This molecular tunneling technique successfully produces a sulfur and nitrogen co-doped soft carbon with expanded interlayer spacing, high ionic conductivity, and improved electronic conductivity. This carbon modification strategy, also demonstrated by Zhou et al.,<sup>[68]</sup> creates numerous defects that enable  $\text{Li}^+$  to hop between carbon layers, providing additional transport pathways. Crucially, the introduced C–N and C–S bonds effectively lower the energy barrier for  $\text{Li}^+$  transport, significantly accelerating its diffusion rate.<sup>[203–206]</sup>

The collective effect of these modifications enables  $\text{Li}^+$  to rapidly diffuse through the soft carbon bulk, where they are reduced to metallic lithium within the carbon matrix. This mechanism of intra-layer lithium plating effectively distributes the deposition sites, drastically reducing the local current density at the SSE interface and preventing the charge accumulation that triggers dendrite growth. By ensuring timely  $\text{Li}^+$  replenishment and homogenizing deposition, this approach presents a robust strategy for stabilizing lithium metal anodes in solid-state batteries.

Wang et al.<sup>[70]</sup> provided direct experimental evidence of the efficacy of their modified soft carbon through scanning electron microscopy (SEM). After depositing  $3 \text{ mAhcm}^{-2}$  of lithium at a high current density of  $4 \text{ mAcm}^{-2}$ , a stark contrast was observed between the unmodified soft carbon (SC) and the thiourea-calcined carbon (SC-TU). The SC-TU anode exhibited a dense, uniform morphology where lithium metal filled all interparticle voids, depositing on the particle surfaces rather than forming isolated dendrites. This homogeneous “gap-filling” deposition mode significantly increases the available deposition sites, effectively reducing the local current density and suppressing dendrite nucleation. In contrast, the unmodified SC anode, with its low  $\text{Li}^+$  diffusion coefficient, forces lithium ions to be reduced directly at the SC/electrolyte interface. This leads to the classical top-down dendrite growth that can penetrate the solid electrolyte. A schematic comparing these two distinct deposition behaviors is provided in Figure 14a–h. Quantitative analysis confirmed the superior kinetics of the SC-TU anode. The  $\text{Li}^+$  diffusion coefficient in SC-TU was measured to be 2–3 times higher than in pristine SC. Furthermore, the exchange current density for the SC-TU-Li system was an order of magnitude greater than that of the SC-Li anode

(Figure 14i,j), unequivocally demonstrating the enhanced electrochemical activity and rapid charge transfer enabled by the modification.

The full cell incorporating the modified anode (LCO/LPSCl/SC-TU-Li) demonstrated exceptional performance, achieving an unprecedented current density of  $15 \text{ mAcm}^{-2}$  with a capacity of  $70 \text{ mAhg}^{-1}$  and an ultra-long cycle life of 12 000 cycles with 95% capacity retention. This stands in stark contrast to the cell with the unmodified soft carbon anode (LCO/LPSCl/SC-Li), whose capacity degraded to zero after only 2000 cycles. The charge/discharge curves of the latter revealed significant polarization and symptoms of micro-short circuits, resulting in a low Coulombic efficiency of merely 40–60%. This failure is attributed to dendritic growth, which accelerates interfacial side reactions and generates “dead Li,” leading to escalating polarization and capacity fade. The remarkable current density of  $15 \text{ mAcm}^{-2}$  achieved by the SC-TU-Li anode far surpasses previously reported levels for all-solid-state batteries. This enhancement is directly linked to the S/N co-doping and expanded interlayer spacing, which collectively widen and optimize the  $\text{Li}^+$  transport channels, thereby drastically improving ionic diffusion. Beyond rate capability, the SC-TU-Li anode also exhibited superior areal capacity. As shown in Figure 14k,l, the LCO/LPSCl/SC-TU-Li cell maintained 93.8% of its capacity over 200 cycles at a high areal capacity of  $3 \text{ mAhcm}^{-2}$  and a current density of  $6 \text{ mAcm}^{-2}$ , underscoring its potential for high-energy, fast-charging applications.

Phase-field modeling of the SC-TU anode elucidated the origin of its high diffusion coefficient and exchange current density. The simulations confirmed that the ionic diffusion coefficient in SC-TU is three times greater than in unmodified SC, enabling  $\text{Li}^+$  to permeate more rapidly into its expanded interlayers. Consequently, the concentration of  $\text{Li}^+$  ( $C_{\text{Li}^+}$ ) within the SC-TU bulk is significantly higher. Coupled with this, the high exchange current density of SC-TU allows these internal  $\text{Li}^+$  ions to combine rapidly with electrons to form metallic lithium within the carbon matrix, rather than at the solid-state electrolyte interface. This mechanism prevents the dangerous charge accumulation that triggers dendrite formation. In essence, the large transport channels in SC-TU facilitate the stable deposition of lithium in a dense, multi-layer structure, enabling rapid diffusion and plating without the formation of dendrites.

## 6. Carbon Spheres

Carbon spheres represent a highly promising class of materials for advanced alkali-ion battery anodes, owing to their tunable porosity and morphology.<sup>[207–209]</sup> A key advancement was demonstrated by Ye et al.,<sup>[69]</sup> who showed that engineering conductive mesochannels within these spheres drastically enhances their electrochemical properties. Specifically, constructing small through-holes in hollow carbon spheres creates a continuous and uninterrupted internal surface area, which significantly promotes the surface-mediated diffusion of ions. However, mass transport within such nanoconfined spaces is complex, being highly sensitive to pore size, geometry, connectivity, and ion species. To unravel this complexity, Ye et al.<sup>[69]</sup> undertook a combined experimental and theoretical investigation of sodium-ion diffusion in model hollow carbon capsules. Through precise pore

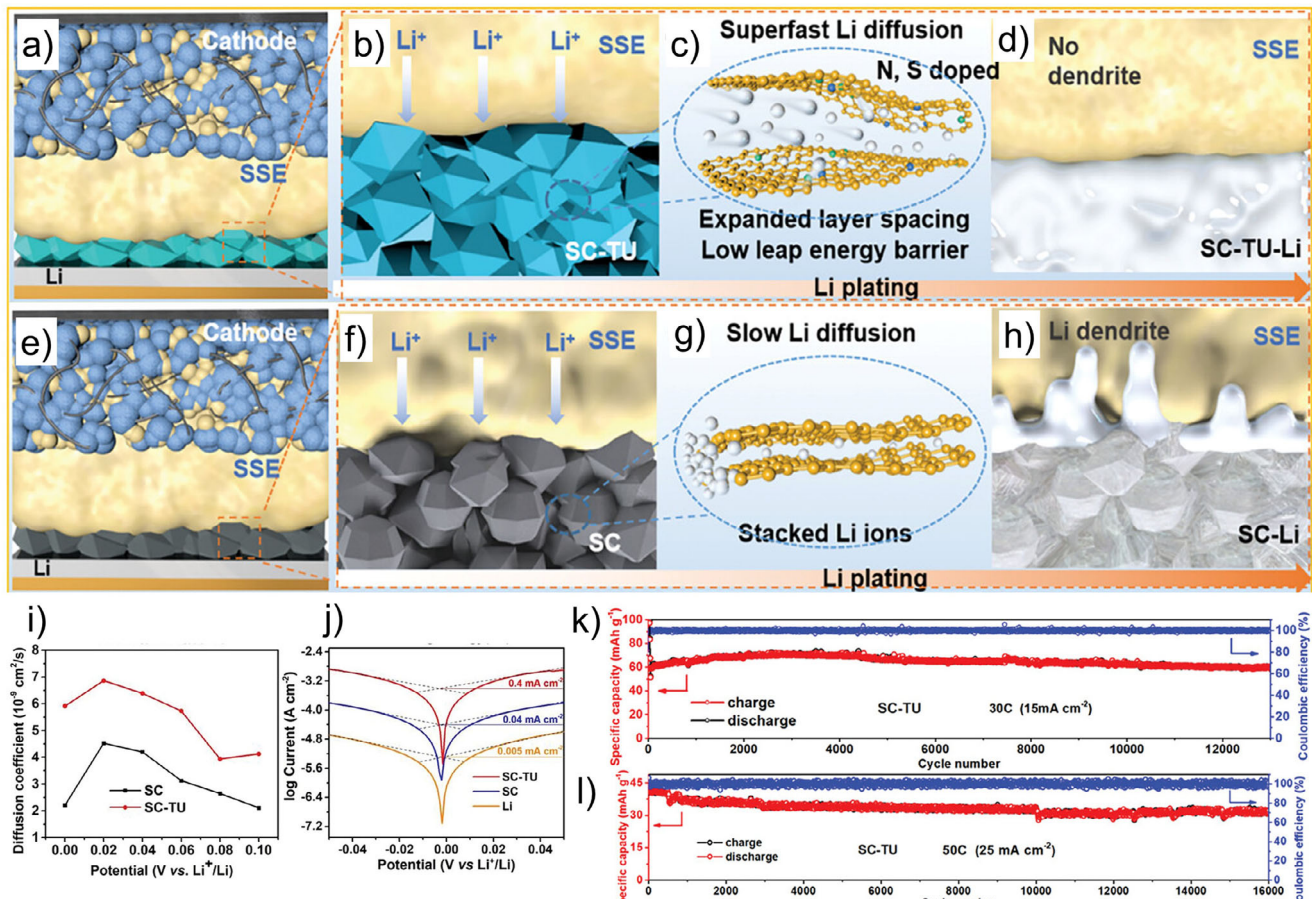


**Figure 14.** Schematic illustration of Li deposition for (a–d) SC-TU and (e–h) SC anodes. i)  $\text{Li}^+$  diffusion coefficient of SC and SC-TU. j) Tafel curves of Li symmetric cells with different interlayers. Cycling performance of LCO-LPSCI-SC-TU/Li ASSB and at k) 30 C and l) 50 C. Reproduced with permission,<sup>[70]</sup> 2024, John Wiley & Sons Inc.

engineering, they introduced directional open mesochannels, which were then directly observed to facilitate enhanced Na transport via *in situ* transmission electron microscopy. This architectural modification increased the available electroactive surface area by approximately an order of magnitude, thereby providing abundant, efficient pathways for rapid surface diffusion of sodium ions.

Two model structures were selected for this study: hollow carbon spheres with disconnected micropores (DMSs) and those with open mesochannels (OMSs), as schematically illustrated in Figure 15a. The introduction of mesochannels endowed the OMSs with an ultra-high accessible surface area, approximately nine times greater than that of the DMSs (Figure 15b). *In situ* sodium plating experiments on individual spheres were conducted to elucidate the Na transport and deposition behavior. For the DMSs, sodium metal plated exclusively on the outer surface, with the carbon shell thickness remaining constant. This indicates that the microporous walls impeded bulk diffusion, preventing significant sodiation of the shell.<sup>[210–213]</sup> Continued plating led to a thick, irregular, and dendritic Na coating (Figure 15c). In stark contrast, the open mesochannels in OMSs provided efficient pathways for Na ions to access the interior. The plating process on OMSs occurred in three distinct stages: 1) sodiation

of the carbon shell via rapid surface diffusion, 2) filling of the mesochannels with metallic Na, and 3) rapid filling of the internal cavity once the channels were blocked by deposited Na. This mechanism resulted in 92% of OMSs efficiently encapsulating sodium within their cavities, compared to only 5% for DMSs. Furthermore, quantitative analysis revealed the Na deposition rate in OMSs ( $2.07 \times 10^6 \text{ nm}^3 \text{s}^{-1}$ ) was an order of magnitude faster than in DMSs ( $0.21 \times 10^6 \text{ nm}^3 \text{s}^{-1}$ ).

To elucidate the dominant transport mechanism for sodium within these structures, three potential pathways were evaluated, as depicted in Figure 15e: 1) bulk diffusion through the carbon layer, 2) bulk diffusion through metallic sodium, and 3) interfacial diffusion along the Na-C boundary. DFT calculations by Ye et al. quantified the energy barriers for these pathways.<sup>[69]</sup> The barrier for bulk Na diffusion was found to be 0.64 eV (Pathway I), while diffusion within the graphite interlayers was 0.37 eV (Pathway II). In stark contrast, the barrier for interfacial diffusion (Pathway III) was only 0.09 eV—approximately 4 and 7 times lower than the other two pathways, respectively (Figure 15f,h). This remarkably low barrier is even superior to surface diffusion on graphene (0.16 eV), confirming that interfacial diffusion, a process analogous to Coble creep,<sup>[214]</sup> is the dominant and most efficient transport mechanism. This theoretical finding was

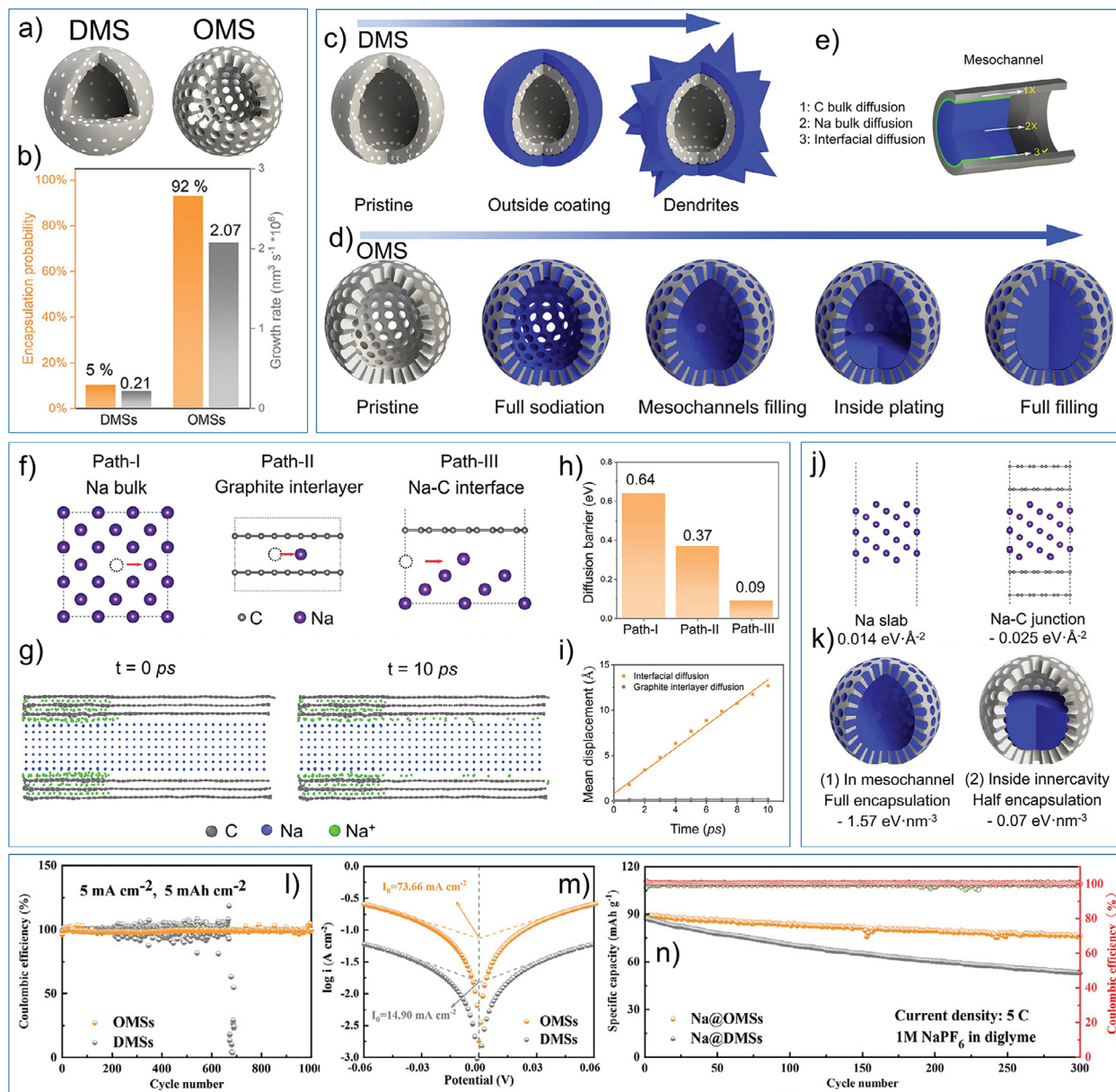


**Figure 15.** a) Schematic illustration of DMSs and OMSs. b) Histogram statics of encapsulation probability and Na growth rate on DMSs and OMSs. c) Schematic Na plating on a DMS leads to Na coating and dendrite-like growth on the outer surface. d) Schematic Na filling of a pristine OMS through a three-stage process, shell sodiation, mesochannel filling, and cavity filling. e) Schematic illustration of the Na diffusion mechanism in a Na-filled mesochannel. f) Na migration pathways, i.e., Na bulk, graphite interlayer, and Na-C interface and (h) the corresponding diffusion energy barriers. g) Snapshots of MD simulations of Na diffusion in a mesochannel and (i) the corresponding migration mean displacement of Na<sup>+</sup> versus MD simulation time. j) Optimized structures of a Na slab and a junction between Na metal and graphene. k) Simplified models showing Na plating with the same volume in regions 1-2, i.e., the open mesochannels and inner cavity. Comparison of the electrochemical performances between DMSs- and OMSs-based electrodes, l) Coulombic efficiency at 5 mAcm<sup>-2</sup> and 5 mAhcm<sup>-2</sup>, m) Tafel curves of symmetric cells, n) Cycling performance of Na || PB full cells. Reproduced with permission,<sup>[69]</sup> 2023, John Wiley & Sons Inc.

corroborated by molecular dynamics (MD) simulations, which demonstrated rapid sodium movement along the Na-C interface within 10 ps, while Na confined between carbon layers remained largely immobile (Figure 15i). Furthermore, DFT analysis revealed that sodium deposition within the mesochannels is energetically more favorable than in the hollow cavity (Figure 15j,k). This energetically driven sequence—where Na preferentially fills

the mesochannels before accumulating in the central cavity—provides a theoretical foundation for the three-step deposition process (shell sodiation, channel filling, cavity filling) directly observed via *in situ* TEM.<sup>[69]</sup>

The study further demonstrated that metallic potassium can be effectively encapsulated within OMS hosts via a similar three-step mechanism. However, the kinetics differ notably from those

of sodium: the initial potassiation of the carbon shells was significantly slower, attributable to the inherently slower surface diffusion of K ions. In contrast, the final cavity-filling stage was strikingly rapid; the internal cavity was filled with metallic K in less than 0.2 s and stripped in just 1.2 s. This indicates that once a continuous metallic pathway is established by filling the mesochannels, both Na and K can be shuttled into and out of the host's interior with exceptional speed, ensuring a uniform metal supply and dissolution. These results collectively affirm that interfacial diffusion along the metal–carbon boundary provides a highly efficient pathway for alkali metal transport.<sup>[69]</sup>

A direct comparison of the cycling performance unequivocally demonstrates the superiority of the OMS electrode over its DMS counterpart. At a high current density of  $5 \text{ mA cm}^{-2}$  and an areal capacity of  $5 \text{ mAh cm}^{-2}$ , the OMS electrode exhibits significantly superior cycling stability and Coulombic efficiency (Figure 15*l*). This enhanced stability is attributed to the vast accessible surface area provided by the mesochannels, which promotes uniform  $\text{Na}^+$  transport and deposition. In contrast, the rapid failure of the DMS electrode is a direct consequence of slow ion diffusion, leading to dendritic growth. This kinetic advantage is further quantified by Tafel analysis, which reveals a much higher exchange current density for the OMSs@Na electrode ( $73.66 \text{ mA cm}^{-2}$ ) compared to the DMSs@Na ( $114.90 \text{ mA cm}^{-2}$ ), indicating significantly faster charge transfer kinetics (Figure 15*m*). In full-cell configurations with a Prussian blue cathode, the OMS-based cell demonstrated markedly better capacity retention at a 5C rate and superior rate performance compared to the DMS-based cell (Figure 15*n*). A recognized limitation, however, is the suboptimal rate capability stemming from poor electrical contact between the 0D nanospheres.<sup>[215]</sup> To overcome this, the pore-engineering strategy was successfully extended to 1D nanotubes and 2D nanosheets. In situ TEM studies confirmed that this architectural modification universally enables fast Na transfer and deposition kinetics across different carbon nanomaterial dimensions.<sup>[69]</sup> Notably, anodes based on 2D carbon nanosheets achieved exceptional cyclability at ultra-high current densities of  $30 \text{ mA cm}^{-2}$  with a capacity of  $10 \text{ mAh cm}^{-2}$ , ranking among the best performances reported to date. The strategy's versatility can be further enhanced by combining pore engineering with chemical modification, such as atomic doping with Sn, Zn, or Fe,<sup>[216,217]</sup> which is expected to simultaneously improve electrode kinetics and stability against alkali metals. In summary, the introduction of open mesochannels accelerates Na plating by approximately an order of magnitude, enabling outstanding performance at extreme current densities. This establishes pore engineering as a versatile and effective foundational strategy for developing high-performance alkali metal batteries by fundamentally overcoming transport limitations.

## 7. Conclusion and Perspectives

Graphite and other carbon materials will remain the main anode materials Li-ion batteries for decades to come. Researchers in industry and academia are working to develop more advanced carbon-based anodes with better performance. These include higher rate capability and energy density, lower first cycle irreversible capacity loss, longer cycle life, and better safety performance. One of the directions for improving the performance of

ion batteries is the formation of alkali metal multilayer structures in carbon-based anode hosts. Multilayer structures of alkali metals in carbon-based anodes increase the anode capacity and accelerate the charging rate. Contrary to the widespread belief that alkali metal atoms intercalated in layered materials only form monolayer structures, in 2018 have shown that multi-layer configurations of lithium are possible in bilayer graphene<sup>[28]</sup> and it initiated a new line of research into the intercalation of alkali metals in carbon-based materials. Furthermore, the possibility of forming multilayer configurations K, Rb, Cs in bilayer graphene was theoretically predicted and experimentally demonstrated. It has been shown that high capacity and fast charging in hard carbon based anodes is also related to the formation of multilayer configurations in the pores of hard carbon. Modification of graphite and soft carbon by creating atomic channels and increasing the interlayer distance leads to the formation of multi-layer configurations of lithium and consequently to fast diffusion of superdense Li without dendrite formation. It has also been shown experimentally that the introduction of open mesochannels in carbon spheres leads to more stable dendrite-free cycling of Na with high rate characteristics due to the formation and diffusion of Na multilayer structures in the mesochannels of the carbon sphere.

Despite the successes of research into the formation of multilayer structures in carbon-based host materials, there are still many problems to be solved before these developments can be translated into working devices. In particular, there is a need to improve imaging techniques of the processes taking place in the material. Multilayer configurations of lithium between graphene layers were experimentally detected in 2018,<sup>[28]</sup> and only in 2024 was the growth process of 2D lithium crystals between graphene layers was visualized and it was determined that the growth occurs on graphene vacancies.<sup>[77]</sup> To improve hard carbon-based anode materials, it is necessary to understand in detail the mechanism underlying the storage of various alkali metal ions in the pores of hard carbon.<sup>[218]</sup> In the process of modification of graphene<sup>[68]</sup> and soft carbon<sup>[70]</sup> by molecular tunnelling methods, it is necessary to understand what size of atomic channels is the most effective for diffusion and storage of alkali metal ions. When carbon spheres are used as anodes,<sup>[69]</sup> difficulties with rate performance due to poor contact between nanospheres, and can be solved by improving synthesis methods.

The successful synthesis, study and application of a high capacity, fast charging carbon based ion battery requires attention to a number of critical areas:

### 1) Theoretical Simulations.

The application of quantum chemistry, machine learning and molecular dynamics methods will allow reliable estimation of thermodynamic, mechanical and kinetic properties of ion battery materials.<sup>[219]</sup> An important advantage of this approach is the ability to predict the properties of compounds that have not yet been studied experimentally, the synthesis and analysis of which can be a time- and material-intensive task. In particular in 2023 it was shown theoretically<sup>[30]</sup> by the DFT method that the growth of 2D Li crystals between graphene layers occurs on vacancies, which was shown experimentally<sup>[77]</sup> a year later in 2024.

However, there are still significant challenges in accurately simulating carbon materials in ion batteries due to computational limitations, especially as the scenario becomes more dynamic and less crystalline. Also the theoretical study of the storage and diffusion of alkali metal atoms in carbon-based materials can be associated with scale problems, as it is often necessary to model structures consisting of several thousand atoms, which is difficult to do with quantum accuracy. Recently, machine learning interatomic potentials have been actively used for large-scale simulations of crystal and non-crystalline structures and complex phenomena, as they allow a balance between quantum accuracy and computational power.<sup>[220]</sup> The effectiveness of machine learning interatomic potentials in the study of battery materials has recently been demonstrated, in particular the calculation of ionic conductivity in structures of a few thousand atoms with DFT accuracy.<sup>[221–223]</sup> Moreover, advanced artificial intelligence models allow scientists to predict migration barriers of Li inside the anode material, significantly accelerating high-throughput screenings of new ionic conductors.<sup>[224]</sup> Using artificial intelligence to speed up the discovery of new materials could significantly speed up the process of creating high-performance ion batteries. A recent study by Google's DeepMind group<sup>[225]</sup> used artificial intelligence to analyze ≈421 000 structures, including 381 000 new ones, many of which could potentially be used in batteries.

## 2) Experimental Technique.

Battery performance is directly related to the intrinsic properties of materials, and to develop commercially efficient ionic batteries it is essential to observe and understand the processes that occur at the atomic level. Therefore, various experimental techniques (SEM, TEM, Raman, XRD, SXAS, FTIR, mass spectroscopy, NMR spectroscopy, etc.) are actively developed and applied to study materials,) are being actively developed and applied to study the materials in Li-ion batteries and to understand the processes that occur during charging/discharging.<sup>[226–234]</sup> In particular, advanced imaging techniques are powerful tools for *in situ* or *ex situ* monitoring of the evolution of the microstructure, crystal structure, interface and chemical reactions of electrode materials, and thus for analyzing the mechanisms within the ion battery. Recent advances in the various imaging techniques used in the ion battery have enabled researchers to directly characterize many detailed electrochemical features of the electrodes, electrolytes, SEIs and internal gases that were not clear in the past. Based on reliable data from measurements, new theories for Li-ion and other rechargeable batteries have been developed, which have helped developers to rationally design key materials, cells, modules and systems, and even their manufacturing processes, in order to balance energy density, specific performance, lifetime, safety and cost.

Although much progress has been made in recent years with the rapid development and commercialization of advanced tools, it is desirable to further develop imaging techniques with specialization, functionalization and simplification for widespread use in ion battery applications. The resolution limit should be further increased, e.g. STM, AFM and Cs-corrected TEM have already reached subatomic resolution, but these techniques are only applicable to specialised sam-

ples, which are usually not the real ones from the practical battery. Cryo-TEM greatly extends the range of high-resolution TEM applications, and many lithium dendrites and subnanostructures associated with SEI are now visible in cryo-TEM. However, despite significant progress in the development of ion battery visualization techniques, there are still major fundamental barriers to obtaining reliable information on battery performance during the charging/discharging process. For *in situ* or *in operando* studies, special cells are created that are far removed from the real-life scenarios of ion battery applications. For example, *in situ* cells for TEM studies require much higher voltages than commonly used cells to drive the electrochemical reactions, which may lead to some deviation in understanding. Therefore, it remains relevant to develop more efficient imaging techniques while improving the validity of the *in situ* generated cells. Integration of multiple imaging techniques is an effective strategy where several imaging techniques are combined in one instrument so that all structural and electrochemical features can be collected simultaneously, which will greatly help us to comprehensively study the mechanisms of ion battery operation.<sup>[227]</sup>

The development of solid-state Nuclear Magnetic Resonance (ssNMR) techniques has made it possible to effectively study the storage mechanisms, phase structure evolution, interfacial composition analysis and intercalation dynamics of alkali metal atoms in carbon-based ion batteries.<sup>[226]</sup> Fundamental single-pulse and *operando* ssNMR experiments make it possible to study the pore filling processes in hard carbons, helping to develop strategies for pore structure design and carbonisation process, which can effectively enhance the filling capacity. In addition, the reversible transformation of active phases in electrochemical cycles and the formation and evolution of dendrites can be clearly observed in ssNMR experiments, providing researchers with useful information for sorting out highly active phases in electrode materials and suppressing dendrite damage. Therefore, it is necessary to promote advanced NMR tools not only for basic chemical analysis, but also to obtain interesting and important dynamic and spatial information. The application of NMR to battery research will undoubtedly help to understand the degradation mechanism and solve fundamental problems, thereby improving the technology to meet the requirements of higher efficiency, longer life and lower cost to accelerate the practical application of ion batteries.

## 3) Synthesis.

Improvement of methods of synthesis of carbon materials with well-controlled properties is the key to successful creation of high capacity and fast charging ion batteries. For example, graphene is a promising material as an anode, but due to its low specific capacitance and tendency to stick together during electrode fabrication, there are problems in its application in ion batteries. Therefore, methods are being developed to transform 2D graphene into a 3D interconnected porous framework with a well-defined hierarchical structure, which can significantly improve electrical conductivity. And the porous structure provides more active sites for rapid electron/ion transfer, and increases mechanical strength to buffer volume expansion during cycling. The storage capacity of alkali metal atoms can be further enhanced by introducing

defects and heteroatoms into graphene sheets by changing the physicochemical and electronic properties and increasing the number of active sites. However, there are still problems related to the control of graphene doping that need to be addressed. Modification of bulk graphite by method of molecular tunnelling to create atomic conducting channels has shown its effectiveness in creating anode material of high capacity and charging rate, but further improvements of the modification method are needed to accurately control the size of atomic channels.

Synthesis parameters are important in the development of hard carbon anode materials because the morphology of the hard carbon, which affects the electrochemical performance, is mainly inherited from the precursors. For example biomass-derived hard carbon is cheap and easy to scale up, but has a complex composition and impurities that complicate the understanding of the charge/discharge process and significantly affect the anode capacity. On the other hand polymeric precursors allow precise control of the composition and morphology of the hard carbon structure but can be complicated and expensive to scale up. Finding a suitable solid carbon precursor will therefore enable the synthesis of high-performance hard carbon anodes in a cost effective and environmentally friendly manner.

Thus, the development of research and synthesis methods will make it possible to create materials with the necessary properties for high-capacity and fast-charging ion batteries. Only complex application of methods of theoretical modelling and experimental research will allow to determine important parameters of materials, which should be changed at the stage of synthesis.

#### 4) Economic and Scalability Considerations.

While the scientific advances in forming multilayer alkali metal structures are promising, their translation into commercially viable technologies hinges on overcoming significant economic and scalability challenges in material preparation. The molecular tunneling technique used to create atomic channels in graphite and soft carbon, while demonstrably effective, presents scalability concerns. The process relies on precise thermal treatment in a controlled ammonia ( $\text{NH}_3$ ) environment. Large-volume production would require sophisticated reactor systems to ensure uniform gas concentration and flow, impacting both capital and operational expenditures. Furthermore, the use of  $\text{NH}_3$  necessitates stringent safety protocols and gas handling systems, adding to the complexity and cost. Future research must focus on simplifying this process, potentially by exploring alternative etching agents or developing more cost-effective and safer catalytic tunneling methods.

Similarly, the synthesis of high-performance hard carbon anodes faces a critical bottleneck in precursor consistency. While biomass-derived hard carbon is cheap and sustainable, its complex and variable composition leads to inconsistent electrochemical performance, complicating mass production. Polymer-derived hard carbon offers superior control over morphology and composition but at a higher cost that may be prohibitive for large-scale applications like grid storage. There is an urgent need to identify and standardize low-cost, abundant precursors with re-

producible properties, or to develop robust, low-energy synthesis pathways that can tolerate precursor variability while delivering consistent pore structure and performance.

Addressing these economic and manufacturing bottlenecks is as crucial as the fundamental material research to ensure that these high-capacity, fast-charging carbon-based anodes can make a tangible impact on the energy storage market.

#### Conflict of Interest

The authors declare no conflict of interest.

#### Keywords

fast charging, high capacity, metal-ion battery, multilayers alkali metal structures

Received: July 14, 2025

Revised: October 14, 2025

Published online:

- [1] M. Li, J. Lu, Z. Chen, K. Amine, *Adv. Mater.* **2018**, *30*, 1800561.
- [2] P. V. Kamat, *ACS Energy Lett.* **2019**, *4*, 2757.
- [3] C. P. Grey, D. S. Hall, *Nat. Commun.* **2020**, *11*, 6279.
- [4] J. Fleischmann, M. Hanicke, E. Horetsky, D. Ibrahim, S. Jautelat, M. Linder, P. Schaufuss, L. Torscht, A. van de Rijt, *Battery 2030: Resilient, Sustainable, and Circular, McKinsey & Company* **2023**, *2*.
- [5] Y. Liu, H. Shi, Z.-S. Wu, *Energy Environ. Sci.* **2023**, *16*, 4834.
- [6] W. Zhao, C. Zhao, H. Wu, L. Li, C. Zhang, *J. Energy Storage* **2024**, *81*, 110409.
- [7] T. Astles, J. G. McHugh, R. Zhang, Q. Guo, M. Howe, Z. Wu, K. Indykiewicz, A. Summerfield, Z. A. Goodwin, S. Slizovskiy, D. Domaretskiy, A. K. Geim, V. Falko, I. V. Grigorieva, *Nat. Commun.* **2024**, *15*, 6933.
- [8] Y. Dong, Y. Chen, Q. Zeng, J. Feng, M. Fang, Z. Shi, J. Liu, Y. Sheng, X. Yue, Z. Liang, *Energy Mater. Adv.* **2024**, *5*, 0113.
- [9] T. Wulandari, D. Fawcett, S. B. Majumder, G. E. Poinern, *Battery Energy* **2023**, *2*, 20230030.
- [10] E. Goikolea, V. Palomares, S. Wang, I. R. de Larramendi, X. Guo, G. Wang, T. Rojo, *Adv. Energy Mater.* **2020**, *10*, 2002055.
- [11] A. Zhao, Y. Fang, X. Ai, H. Yang, Y. Cao, *J. Energy Chem.* **2021**, *60*, 635.
- [12] T. Hosaka, K. Kubota, A. S. Hameed, S. Komaba, *Chem. Rev.* **2020**, *120*, 6358.
- [13] T. Li, Q. Zhang, *J. Energy Chem.* **2018**, *27*, 373.
- [14] J. Huang, Y. Chen, Z. Cen, T. Yi, M. Liang, Y. Zhu, R. Liu, R. Fu, S. Liu, D. Wu, *Adv. Mater.* **2024**, *36*, 2403033.
- [15] B. Lu, N. Ru, J. Duan, Z. Li, J. Qu, *ACS Omega* **2023**, *8*, 21842.
- [16] S. Chen, J. Hu, S. Han, Y. Guo, N. Belzile, T. Deng, *Sep. Purif. Technol.* **2020**, *251*, 117340.
- [17] J. Niu, Z. Zhang, D. Aurbach, *Adv. Energy Mater.* **2020**, *10*, 2000697.
- [18] X. Chai, H. Xie, T.-T. Zhang, Y. Xin, F. Zhang, B. He, H. Xie, L. Yu, H. Tian, *Energy Storage Mater.* **2024**, *10*, 103460.
- [19] T. Masese, G. M. Kanyolo, *EcoEnergy* **2024**, *2*, 339.
- [20] A. Taghavi-Kahagh, H. Roghani-Mamaqani, M. Salami-Kalajahi, *J. Energy Chem.* **2024**, *90*, 77.
- [21] A. P. Maltsev, I. V. Chepkasov, A. R. Oganov, *Mater. Today Energy* **2024**, *39*, 101467.
- [22] J. Xu, Y. Dou, Z. Wei, J. Ma, Y. Deng, Y. Li, H. Liu, S. Dou, *Adv. Sci.* **2017**, *4*, 1700146.

- [23] K. Ji, J. Han, A. Hirata, T. Fujita, Y. Shen, S. Ning, P. Liu, H. Kashani, Y. Tian, Y. Ito, J.-i. Fujita, Y. Oyama, *Nat. Commun.* **2019**, *10*, 275.
- [24] F. J. Sonia, M. K. Jangid, B. Ananthoju, M. Aslam, P. Johari, A. Mukhopadhyay, *J. Mater. Chem. A* **2017**, *5*, 8662.
- [25] S. Yuan, Q. Lai, X. Duan, Q. Wang, *J. Energy Storage* **2023**, *61*, 106716.
- [26] A. K. Prajapati, A. Bhatnagar, *J. Energy Chem.* **2023**, *83*, 509.
- [27] I. V. Chepkasov, M. Ghorbani-Asl, Z. I. Popov, J. H. Smet, A. V. Krasheninnikov, *Nano Energy* **2020**, *75*, 104927.
- [28] M. Kühne, F. Börner, S. Fecher, M. Ghorbani-Asl, J. Biskupek, D. Samuelis, A. V. Krasheninnikov, U. Kaiser, J. H. Smet, *Nature* **2018**, *564*, 234.
- [29] I. V. Chepkasov, J. H. Smet, A. V. Krasheninnikov, *J. Phys. Chem. C* **2022**, *126*, 15558.
- [30] X. Zhang, M. Ghorbani-Asl, Y. Zhang, A. V. Krasheninnikov, *Mater. Today Energy* **2023**, *34*, 101293.
- [31] J. Bondareva, D. Chernodubov, A. Mumlyakov, M. Tarkhov, N. Porokhov, K. Maslakov, D. Kvashnin, E. Epifanov, O. Dubinin, I. Krupatin, X. Shi, N. D. Orekhov, F. S. Fedorov, S. A. Evlashin, *Electrochim. Acta* **2025**, *513*, 145522.
- [32] S. Evlashin, F. Fedorov, P. Dyakonov, Y. M. Maksimov, A. Pilevsky, K. Maslakov, Y. O. Kuzminova, Y. A. Mankelevich, E. Voronina, S. Dagesyan, V. A. Pletneva, A. A. Pavlov, M. A. Tarkhov, I. V. Trofimov, V. L. Zhdanov, N. V. Suetin, I. S. Akhatov, *J. Phys. Chem. Lett.* **2020**, *11*, 4859.
- [33] I. V. Chepkasov, V. S. Baidyshev, A. G. Kvashnin, *J. Energy Storage* **2025**, *125*, 116831.
- [34] X. Liu, D. Lyu, C. Merlet, M. J. Leesmith, X. Hua, Z. Xu, C. P. Grey, A. C. Forse, *Science* **2024**, *384*, 321.
- [35] S. A. Evlashin, Y. M. Maksimov, P. V. Dyakonov, A. A. Pilevsky, K. I. Maslakov, Y. A. Mankelevich, E. N. Voronina, S. V. Vavilov, A. A. Pavlov, E. V. Zenova, I. S. Akhatov, N. V. Suetin, *Sci. Rep.* **2019**, *9*, 6716.
- [36] S. Evlashin, F. Fedorov, D. Chernodubov, K. Maslakov, O. Dubinin, R. Khmelnitsky, J. Bondareva, V. Zhdanov, A. Pilevsky, E. Sukhanova, Z. I. Popov, N. V. Suetin, *J. Electroanal. Chem.* **2024**, *956*, 118091.
- [37] G. Yang, X. Li, Z. Guan, Y. Tong, B. Xu, X. Wang, Z. Wang, L. Chen, *Nano Lett.* **2020**, *20*, 3836.
- [38] V. A. Krivchenko, D. M. Itkis, S. A. Evlashin, D. A. Semenenko, E. A. Goodilin, A. T. Rakhimov, A. S. Stepanov, N. V. Suetin, A. A. Pilevsky, P. V. Voronin, *Carbon* **2012**, *50*, 1438.
- [39] L. Li, D. Zhang, J. Deng, Y. Gou, J. Fang, H. Cui, Y. Zhao, M. Cao, *Carbon* **2021**, *183*, 721.
- [40] B. Babu, *Batteries & Supercaps* **2024**, *7*, e202300537.
- [41] K. Mironovich, S. Evlashin, S. Bocharova, M. Yerdauletov, S. Dagesyan, A. Egorov, N. Suetin, D. Itkis, V. Krivchenko, *J. Mater. Chem. A* **2017**, *5*, 18095.
- [42] I. V. Chepkasov, A. V. Krasheninnikov, *Carbon* **2023**, *213*, 118190.
- [43] H. Zhang, Y. Yang, D. Ren, L. Wang, X. He, *Energy Storage Mater.* **2021**, *36*, 147.
- [44] H. Azuma, H. Imoto, S. Yamada, K. Sekai, *J. Power Sources* **1999**, *81*, 1.
- [45] N. Takami, A. Satoh, M. Hara, T. Ohsaki, *J. Electrochem. Soc.* **1995**, *142*, 371.
- [46] N. A. Kaskhedikar, J. Maier, *Adv. Mater.* **2009**, *21*, 2664.
- [47] Y. Jiang, J. Jiang, P. Nie, W. Guo, C. Geng, Z. Sun, Y. Fei, Y. Chen, Q. Zhuang, Z. Xing, Z. Ju, H. Shao, *J. Energy Storage* **2023**, *72*, 108484.
- [48] N. Li, D. Su, *Carbon Energy* **2019**, *1*, 200.
- [49] Y. Nishi, *Chem. Rec.* **2001**, *1*, 406.
- [50] K. Mizushima, P. C. Jones, P. J. Wiseman, J. B. Goodenough, *Mater. Res. Bull.* **1980**, *15*, 783.
- [51] P. Meister, H. Jia, J. Li, R. Kloepsch, M. Winter, T. Placke, *Chem. Mater.* **2016**, *28*, 7203.
- [52] V. Etacheri, R. Marom, R. Elazari, G. Salitra, D. Aurbach, *Energy Environ. Sci.* **2011**, *4*, 3243.
- [53] A. Yacoby, *Nat. Phys.* **2011**, *7*, 925.
- [54] Y. Guo, Y. Wei, H. Li, T. Zhai, *Small* **2017**, *13*, 1701649.
- [55] K. Fredenhagen, G. Cadenbach, *Z. Anorg. Allg. Chem.* **1926**, *158*, 249.
- [56] R. C. Massé, C. Liu, Y. Li, L. Mai, G. Cao, *Natl. Sci. Rev.* **2017**, *4*, 26.
- [57] M. S. Whittingham, *Chem. Rev.* **2014**, *114*, 11414.
- [58] M. Winter, J. O. Besenhard, M. E. Spahr, P. Novak, *Adv. Mater.* **1998**, *10*, 725.
- [59] C.-M. Park, J.-H. Kim, H. Kim, H.-J. Sohn, *Chem. Soc. Rev.* **2010**, *39*, 3115.
- [60] F. Wu, G. Yushin, *Energy Environ. Sci.* **2017**, *10*, 435.
- [61] F. Klein, B. Jache, A. Bhide, P. Adelhelm, *Phys. Chem. Chem. Phys.* **2013**, *15*, 15876.
- [62] M. Lao, Y. Zhang, W. Luo, Q. Yan, W. Sun, S. X. Dou, *Adv. Mater.* **2017**, *29*, 1700622.
- [63] I. Sultana, M. M. Rahman, Y. Chen, A. M. Glushenkov, *Adv. Funct. Mater.* **2018**, *28*, 1703857.
- [64] H. Cheng, J. G. Shapter, Y. Li, G. Gao, *J. Energy Chem.* **2021**, *57*, 451.
- [65] W. Li, X. Qian, S. Hou, X. Xia, D. He, J. Xia, G. He, H. Chen, *J. Energy Storage* **2024**, *99*, 113188.
- [66] J. Wang, L. Xi, C. Peng, X. Song, X. Wan, L. Sun, M. Liu, J. Liu, *Adv. Eng. Mater.* **2024**, *26*, 2302063.
- [67] A. K. Mishra, B. S. Patial, Monika, *Mater. Today Electron.* **2024**, *100089*.
- [68] S. Zhou, W. Chen, J. Shi, G. Li, F. Pei, S. Liu, W. Ye, L. Xiao, M.-S. Wang, D. Wang, Y. Qiao, L. Huang, G.-L. Xu, H.-G. Liao, J.-F. Chen, K. Amine, S.-G. Sun, *Energy Environ. Sci.* **2022**, *15*, 196.
- [69] W. Ye, X. Li, B. Zhang, W. Liu, Y. Cheng, X. Fan, H. Zhang, Y. Liu, Q. Dong, M.-S. Wang, *Adv. Mater.* **2023**, *35*, 2210447.
- [70] Z. Wang, Z. Mu, T. Ma, W. Yan, D. Wu, M. Yang, J. Peng, Y. Xia, S. Shi, L. Chen, H. Li, F. Wu, *Adv. Mater.* **2024**, *36*, 2310395.
- [71] Y.-C. Lin, R. Matsumoto, Q. Liu, P. Solís-Fernández, M.-D. Siao, P.-W. Chiu, H. Ago, K. Suenaga, *Nat. Commun.* **2024**, *15*, 425.
- [72] F. J. Sonia, M. K. Jangid, B. Ananthoju, M. Aslam, P. Johari, A. Mukhopadhyay, *J. Mater. Chem. A* **2017**, *5*, 8662.
- [73] S. Yang, S. Li, S. Tang, W. Dong, W. Sun, D. Shen, M. Wang, *Theor. Chem. Acc.* **2016**, *135*, 1.
- [74] E. Lee, K. A. Persson, *Nano Lett.* **2012**, *12*, 4624.
- [75] C. Zhang, K. L. Firestein, J. F. Fernando, D. Siriwardena, J. E. von Treifeldt, D. Golberg, *Adv. Mater.* **2020**, *32*, 1904094.
- [76] M. Kühne, F. Paolucci, J. Popovic, P. M. Ostrovsky, J. Maier, J. H. Smet, *Nat. Nanotechnol.* **2017**, *12*, 895.
- [77] Y. Li, F. Börner, M. Ghorbani-Asl, J. Biskupek, X. Zhang, Y. Zhang, D. Bresser, A. V. Krasheninnikov, U. Kaiser, *Adv. Funct. Mater.* **2024**, *34*, 2406034.
- [78] J. C. Meyer, F. Eder, S. Kurasch, V. Skakalova, J. Kotakoski, H. J. Park, S. Roth, A. Chuvalin, S. Eyhusein, G. Benner, A. V. Krasheninnikov, U. Kaiser, *Phys. Rev. Lett.* **2012**, *108*, 196102.
- [79] S. Riikonen, A. Krasheninnikov, L. Halonen, R. Nieminen, *J. Phys. Chem. C* **2012**, *116*, 5802.
- [80] M. Liu, A. Kutana, Y. Liu, B. I. Yakobson, *J. Phys. Chem. Lett.* **2014**, *5*, 1225.
- [81] K. Doll, N. Harrison, V. Saunders, *J. Phys.: Condens. Matter* **1999**, *11*, 5007.
- [82] S. N. Shirodkar, E. Kaxiras, *Phys. Rev. B* **2016**, *93*, 245438.
- [83] J. Zhou, W. Zhou, C. Guan, J. Shen, C. Ouyang, M. Lei, S. Shi, W. Tang, *Sci. China Phys. Mech. Astron.* **2012**, *55*, 1376.
- [84] C. Hartwigsen, W. Witschel, E. Spohr, *Phys. Rev. B* **1997**, *55*, 4953.
- [85] R. F. Bader, *Acc. Chem. Res.* **1985**, *18*, 9.
- [86] W. Tang, E. Sanville, G. Henkelman, *J. Phys.: Condens. Matter* **2009**, *21*, 084204.
- [87] H. Moriwake, A. Kuwabara, C. A. Fisher, Y. Ikuhara, *RSC Adv.* **2017**, *7*, 36550.

- [88] Y. Liu, B. V. Merinov, W. A. Goddard III, *Proc. Natl. Acad. Sci. USA* **2016**, *113*, 3735.
- [89] B. Olinger, J. Shaner, *Science* **1983**, *219*, 1071.
- [90] M. I. McMahon, R. J. Nelmes, *Chem. Soc. Rev.* **2006**, *35*, 943.
- [91] V. F. Degtyareva, *Solid State Sci.* **2014**, *36*, 62.
- [92] K. Takemura, K. Syassen, *Phys. Rev. B* **1983**, *28*, 1193.
- [93] H. T. Hall, L. Merrill, J. D. Barnett, *Science* **1964**, *146*, 1297.
- [94] K. Takemura, S. Minomura, O. Shimomura, *Phys. Rev. Lett.* **1982**, *49*, 1772.
- [95] S. Carlesi, A. Franchini, V. Bortolani, S. Martinelli, *Phys. Rev. B* **1999**, *59*, 11716.
- [96] K. Chang, W. Chen, *Chem. Commun.* **2011**, *47*, 4252.
- [97] K. Chang, W. Chen, *ACS nano* **2011**, *5*, 4720.
- [98] K. Chang, W. Chen, L. Ma, H. Li, H. Li, F. Huang, Z. Xu, Q. Zhang, J.-Y. Lee, *J. Mater. Chem.* **2011**, *21*, 6251.
- [99] R. I. Pushparaj, D. Cakir, X. Zhang, S. Xu, M. Mann, X. Hou, *ACS Appl. Mater. Interfaces* **2021**, *13*, 59950.
- [100] D. Wang, S. Li, A. Liu, J. Yuan, Y. Cao, Z. Shi, *J. Phys. Chem. Solids* **2024**, *193*, 112172.
- [101] C. Liu, Y. Bai, Y. Zhao, H. Yao, H. Pang, *Energy Storage Mater.* **2020**, *33*, 470.
- [102] K. Shiva, H. R. Matte, H. Rajendra, A. J. Bhattacharyya, C. Rao, *Nano Energy* **2013**, *2*, 787.
- [103] T. D. Thanh, N. D. Chuong, H. Van Hien, T. Kshetri, N. H. Kim, J. H. Lee, L. H. Tuan, *Prog. Mater. Sci.* **2018**, *96*, 51.
- [104] T. Ahmed, N. Modine, J.-X. Zhu, *Appl. Phys. Lett.* **2015**, *107*, 4.
- [105] R. H. Miwa, W. L. Scopel, *J. Phys.: Condens. Matter* **2013**, *25*, 445301.
- [106] X. Shao, K. Wang, R. Pang, X. Shi, *J. Phys. Chem. C* **2015**, *119*, 25860.
- [107] D. T. Larson, I. Fampiou, G. Kim, E. Kaxiras, *J. Phys. Chem. C* **2018**, *122*, 24535.
- [108] D. Sun, D. Ye, P. Liu, Y. Tang, J. Guo, L. Wang, H. Wang, *Adv. Energy Mater.* **2018**, *8*, 1702383.
- [109] G. Li, D. Luo, X. Wang, M. H. Seo, S. Hemmati, A. Yu, Z. Chen, *Adv. Funct. Mater.* **2017**, *27*, 1702562.
- [110] L. David, R. Bhandavat, G. Singh, *ACS nano* **2014**, *8*, 1759.
- [111] X. Xie, Z. Ao, D. Su, J. Zhang, G. Wang, *Adv. Funct. Mater.* **2015**, *25*, 1393.
- [112] A. Massaro, A. Pecoraro, A. B. Muñoz-García, M. Pavone, *J. Phys. Chem. C* **2021**, *125*, 2276.
- [113] B. Wang, Y. Peng, F. Yuan, Q. Liu, L. Sun, P. Zhang, Q. Wang, Z. Li, Y. A. Wu, *J. Power Sources* **2021**, *484*, 229244.
- [114] J. Zhang, L. Lai, H. Wang, M. Chen, Z. Shen, *Mater. Today Energy* **2021**, *21*, 100747.
- [115] P. Zhang, Y. Yang, X. Duan, S. Zhao, C. Lu, Y. Shen, G. Shao, S. Wang, *Nano Energy* **2020**, *78*, 105352.
- [116] D. Nasr Esfahani, O. Leenaerts, H. Sahin, B. Partoens, F. Peeters, *J. Phys. Chem. C* **2015**, *119*, 10602.
- [117] M. Kan, J. Wang, X. Li, S. Zhang, Y. Li, Y. Kawazoe, Q. Sun, P. Jena, *J. Phys. Chem. C* **2014**, *118*, 1515.
- [118] S. Kretschmer, H.-P. Komsa, P. Bøggild, A. V. Krasheninnikov, *J. Phys. Chem. Lett.* **2017**, *8*, 3061.
- [119] D. K. Bediako, M. Rezaee, H. Yoo, D. T. Larson, S. F. Zhao, T. Taniguchi, K. Watanabe, T. L. Brower-Thomas, E. Kaxiras, P. Kim, *Nature* **2018**, *558*, 425.
- [120] J. S. Kim, J. Kim, J. Zhao, S. Kim, J. H. Lee, Y. Jin, H. Choi, B. H. Moon, J. J. Bae, Y. H. Lee, S. C. Lim, *ACS Nano* **2016**, *10*, 7500.
- [121] R. Kappera, D. Voiry, S. E. Yalcin, B. Branch, G. Gupta, A. D. Mohite, M. Chhowalla, *Nat. Mater.* **2014**, *13*, 1128.
- [122] W. Chen, F. S. Cannon, J. R. Rangel-Mendez, *Carbon* **2005**, *43*, 573.
- [123] Z. Xu, Z. Guo, R. Madhu, F. Xie, R. Chen, J. Wang, M. Tebyetekerwa, Y.-S. Hu, M.-M. Titirici, *Energy Environ. Sci.* **2021**, *14*, 6381.
- [124] L. Suo, Y.-S. Hu, H. Li, M. Armand, L. Chen, *Nat. Commun.* **2013**, *4*, 1481.
- [125] X. Dou, I. Hasa, D. Saurel, C. Vaalma, L. Wu, D. Buchholz, D. Bresser, S. Komaba, S. Passerini, *Mater. Today* **2019**, *23*, 87.
- [126] B. Xiao, T. Rojo, X. Li, *ChemSusChem* **2019**, *12*, 133.
- [127] D. Igarashi, Y. Tanaka, K. Kubota, R. Tatara, H. Maejima, T. Hosaka, S. Komaba, *Adv. Energy Mater.* **2023**, *13*, 2302647.
- [128] X. Dou, I. Hasa, M. Hekmatfar, T. Diemant, R. J. Behm, D. Buchholz, S. Passerini, *ChemSusChem* **2017**, *10*, 2668.
- [129] Y. Li, Y. Lu, Q. Meng, A. C. Jensen, Q. Zhang, Q. Zhang, Y. Tong, Y. Qi, L. Gu, M.-M. Titirici, Y.-S. Hu, *Adv. Energy Mater.* **2019**, *9*, 1902852.
- [130] Z. Li, C. Bommier, Z. S. Chong, Z. Jian, T. W. Surta, X. Wang, Z. Xing, J. C. Neufeind, W. F. Stickle, M. Dolgos, P. A. Greaney, X. Ji, *Adv. Energy Mater.* **2017**, *7*, 1602894.
- [131] D. Stevens, J. Dahn, *J. Electrochem. Soc.* **2000**, *147*, 4428.
- [132] J. T. Robinson, M. K. Zalalutdinov, C. D. Cress, J. C. Culbertson, A. L. Friedman, A. Merrill, B. J. Landi, *ACS nano* **2017**, *11*, 4745.
- [133] P. J. Harris, *Crit. Rev. Solid State Mater. Sci.* **2005**, *30*, 235.
- [134] S. Qiu, L. Xiao, M. L. Sushko, K. S. Han, Y. Shao, M. Yan, X. Liang, L. Mai, J. Feng, Y. Cao, X. Ai, H. Yang, J. Liu, *Adv. Energy Mater.* **2017**, *7*, 1700403.
- [135] X. Lin, Y. Liu, H. Tan, B. Zhang, *Carbon* **2020**, *157*, 316.
- [136] K. Kubota, S. Shimadzu, N. Yabuuchi, S. Tominaka, S. Shiraishi, M. Abreu-Sepulveda, A. Manivannan, K. Gotoh, M. Fukunishi, M. Dahbi, S. Komaba, *Chem. Mater.* **2020**, *32*, 2961.
- [137] V. Palomares, M. Casas-Cabanas, E. Castillo-Martínez, M. H. Han, T. Rojo, *Energy Environ. Sci.* **2013**, *6*, 2312.
- [138] S.-W. Kim, D.-H. Seo, X. Ma, G. Ceder, K. Kang, *Adv. Energy Mater.* **2012**, *2*, 710.
- [139] M. Li, C. Wang, C. Wang, Y. Lyu, J. Wang, S. Xia, J. Mao, Z. Guo, *Adv. Mater.* **2025**, 2416717.
- [140] Y.-S. Hu, Y. Li, *ACS Energy Lett.* **2021**, *6*, 4115.
- [141] T. Perveen, M. Siddiq, N. Shahzad, R. Ihsan, A. Ahmad, M. I. Shahzad, *Renew. Sustain. Energy Rev.* **2020**, *119*, 109549.
- [142] S. Komaba, T. Hasegawa, M. Dahbi, K. Kubota, *Electrochim. Commun.* **2015**, *60*, 172.
- [143] K. Nobuhara, H. Nakayama, M. Nose, S. Nakanishi, H. Iba, *J. Power Sources* **2013**, *243*, 585.
- [144] Y. Li, Y. Lu, P. Adelhelm, M.-M. Titirici, Y.-S. Hu, *Chem. Soc. Rev.* **2019**, *48*, 4655.
- [145] Y. Wang, Y. Chen, J. Xiong, X. Qiu, L. Dong, J. Jiang, X. Kong, Q. Zhuang, Z. Ju, *Chem. Eng. J.* **2024**, 156080.
- [146] L.-F. Zhao, Z. Hu, W.-H. Lai, Y. Tao, J. Peng, Z.-C. Miao, Y.-X. Wang, S.-L. Chou, H.-K. Liu, S.-X. Dou, *Adv. Energy Mater.* **2021**, *11*, 2002704.
- [147] N. LeGe, X.-X. He, Y.-X. Wang, Y. Lei, Y.-X. Yang, J.-T. Xu, M. Liu, X. Wu, W.-H. Lai, S.-L. Chou, *Energy Environ. Sci.* **2023**, *16*, 5688.
- [148] H. Kim, J. C. Hyun, D.-H. Kim, J. H. Kwak, J. B. Lee, J. H. Moon, J. Choi, H.-D. Lim, S. J. Yang, H. M. Jin, D. J. Ahn, K. Kang, H.-J. Jin, H.-K. Lim, Y. S. Yun, *Adv. Mater.* **2023**, *35*, 2209128.
- [149] R. E. Franklin, *Proc. R. Soc. London A* **1951**, *209*, 196.
- [150] L. Ban, D. Crawford, H. Marsh, *J. Appl. Crystallogr.* **1975**, *8*, 415.
- [151] P. J. Harris, *J. Mater. Sci.* **2013**, *48*, 565.
- [152] Y. Chu, J. Zhang, Y. Zhang, Q. Li, Y. Jia, X. Dong, J. Xiao, Y. Tao, Q.-H. Yang, *Adv. Mater.* **2023**, *35*, 2212186.
- [153] D. Stevens, J. Dahn, *J. Electrochem. Soc.* **2000**, *147*, 1271.
- [154] S. Komaba, W. Murata, T. Ishikawa, N. Yabuuchi, T. Ozeki, T. Nakayama, A. Ogata, K. Gotoh, K. Fujiwara, *Adv. Funct. Mater.* **2011**, *21*, 3859.
- [155] B. Zhang, C. M. Ghimbeu, C. Laberty, C. Vix-Guterl, J.-M. Tarascon, *Adv. Energy Mater.* **2016**, *6*, 1501588.
- [156] Y. Cao, L. Xiao, M. L. Sushko, W. Wang, B. Schwenzer, J. Xiao, Z. Nie, L. V. Saraf, Z. Yang, J. Liu, *Nano Lett.* **2012**, *12*, 3783.
- [157] J. Ding, H. Wang, Z. Li, A. Kohandehghan, K. Cui, Z. Xu, B. Zahiri, X. Tan, E. M. Lotfabad, B. C. Olsen, D. Mitlin, *ACS nano* **2013**, *7*, 11004.

- [158] H. Lu, F. Ai, Y. Jia, C. Tang, X. Zhang, Y. Huang, H. Yang, Y. Cao, *Small* **2018**, *14*, 1802694.
- [159] C. Bommier, T. W. Surta, M. Dolgos, X. Ji, *Nano Lett.* **2015**, *15*, 5888.
- [160] P. Bai, Y. He, X. Zou, X. Zhao, P. Xiong, Y. Xu, *Adv. Energy Mater.* **2018**, *8*, 1703217.
- [161] D.-S. Bin, Y. Li, Y.-G. Sun, S.-Y. Duan, Y. Lu, J. Ma, A.-M. Cao, Y.-S. Hu, L.-J. Wan, *Adv. Energy Mater.* **2018**, *8*, 1800855.
- [162] Y. Liu, Y. Wan, J.-Y. Zhang, X. Zhang, C.-T. Hung, Z. Lv, W. Hua, Y. Wang, D. Chao, W. Li, *Small* **2023**, *19*, 2301203.
- [163] M. Anji Reddy, M. Helen, A. Groß, M. Fichtner, H. Euchner, *ACS Energy Lett.* **2018**, *3*, 2851.
- [164] Y. Yang, Z. Liu, Q. Zhang, J. Song, W. Li, S. Jiang, C. Zhang, J. Han, H. Yang, X. Han, S. He, *Adv. Funct. Mater.* **2025**, 14132.
- [165] L. Xie, C. Tang, Z. Bi, M. Song, Y. Fan, C. Yan, X. Li, F. Su, Q. Zhang, C. Chen, *Adv. Energy Mater.* **2021**, *11*, 2101650.
- [166] W. Wang, B. Wang, Y. Li, N. Wang, Y. Xu, C. Wang, Y. Sun, H. Hu, *Chem. - Asian J.* **2024**, *19*, 202301146.
- [167] X.-S. Wu, X.-L. Dong, B.-Y. Wang, J.-L. Xia, W.-C. Li, *Renewable Energy* **2022**, *189*, 630.
- [168] C. d. M. S. Rios, V. Simone, L. Simonin, S. Martinet, C. Dupont, *Biomass Bioenergy* **2018**, *117*, 32.
- [169] X.-X. He, L. Li, X. Wu, S.-L. Chou, *Adv. Mater.* **2025**, 2506066.
- [170] C. Matei Ghimbeu, A. Beda, B. Réty, H. El Marouazi, A. Vizintin, B. Tratnik, L. Simonin, J. Michel, J. Abou-Rjeily, R. Dominko, *Adv. Energy Mater.* **2024**, *14*, 2303833.
- [171] H. Au, H. Alptekin, A. C. Jensen, E. Olsson, C. A. O'Keefe, T. Smith, M. Crespo-Ribadeneyra, T. F. Headen, C. P. Grey, Q. Cai, A. J. Drewb, M.-M. Titirici, *Energy Environ. Sci.* **2020**, *13*, 3469.
- [172] J. S. Weaving, A. Lim, J. Millichamp, T. P. Neville, D. Ledwoch, E. Kendrick, P. F. McMillan, P. R. Shearing, C. A. Howard, D. J. Brett, *ACS Appl. Energy Mater.* **2020**, *3*, 7474.
- [173] T. W. Surta, E. Koh, Z. Li, D. B. Fast, X. Ji, P. A. Greaney, M. R. Dolgos, *Adv. Energy Mater.* **2022**, *12*, 2200647.
- [174] X. Chen, J. Tian, P. Li, Y. Fang, Y. Fang, X. Liang, J. Feng, J. Dong, X. Ai, H. Yang, Y. Cao, *Adv. Energy Mater.* **2022**, *12*, 2200886.
- [175] A. Kamiyama, K. Kubota, D. Igarashi, Y. Youn, Y. Tateyama, H. Ando, K. Gotoh, S. Komaba, *Angew. Chem., Int. Ed.* **2021**, *60*, 5114.
- [176] Y. Youn, B. Gao, A. Kamiyama, K. Kubota, S. Komaba, Y. Tateyama, *npj Comput. Mater.* **2021**, *7*, 48.
- [177] S. Alvin, D. Yoon, C. Chandra, H. S. Cahyadi, J.-H. Park, W. Chang, K. Y. Chung, J. Kim, *Carbon* **2019**, *145*, 67.
- [178] J. M. Stratford, A. K. Kleppe, D. S. Keeble, P. A. Chater, S. S. Meysami, C. J. Wright, J. Barker, M.-M. Titirici, P. K. Allan, C. P. Grey, *J. Am. Chem. Soc.* **2021**, *143*, 14274.
- [179] R. Morita, K. Gotoh, M. Fukunishi, K. Kubota, S. Komaba, N. Nishimura, T. Yumura, K. Deguchi, S. Ohki, T. Shimizu, H. Ishida, *J. Mater. Chem. A* **2016**, *4*, 13183.
- [180] J. M. Stratford, P. K. Allan, O. Pecher, P. A. Chater, C. P. Grey, *Chem. Commun.* **2016**, *52*, 12430.
- [181] A. Vasileiadis, Y. Li, Y. Lu, Y.-S. Hu, M. Wagemaker, *ACS Appl. Energy Mater.* **2022**, *6*, 127.
- [182] Q. Li, X. Liu, Y. Tao, J. Huang, J. Zhang, C. Yang, Y. Zhang, S. Zhang, Y. Jia, Q. Lin, Y. Xiang, J. Cheng, W. Lv, F. Kang, Y. Yang, Q.-H. Yang, *Natl. Sci. Rev.* **2022**, *9*, nwac084.
- [183] K.-H. Chen, V. Goel, M. J. Namkoong, M. Wied, S. Müller, V. Wood, J. Sakamoto, K. Thornton, N. P. Dasgupta, *Adv. Energy Mater.* **2021**, *11*, 2003336.
- [184] A. Rudola, C. J. Wright, J. Barker, *J. Electrochem. Soc.* **2021**, *168*, 110534.
- [185] Y. Li, A. Vasileiadis, Q. Zhou, Y. Lu, Q. Meng, Y. Li, P. Ombrini, J. Zhao, Z. Chen, Y. Niu, X. Qi, F. Xie, R. van der Jagt, S. Ganapathy, M.-M. Titirici, H. Li, L. Chen, M. Wagemaker, Y.-S. Hu, *Nat. Energy* **2024**, *9*, 134.
- [186] D. Saurel, B. Orayech, B. Xiao, D. Carriazo, X. Li, T. Rojo, *Adv. Energy Mater.* **2018**, *8*, 1703268.
- [187] D. Chen, W. Zhang, K. Luo, Y. Song, Y. Zhong, Y. Liu, G. Wang, B. Zhong, Z. Wu, X. Guo, *Energy Environ. Sci.* **2021**, *14*, 2244.
- [188] Y. Li, Y. Lu, L. Chen, Y.-S. Hu, *Chin. Phys. B* **2020**, *29*, 048201.
- [189] Z. Zou, N. Ma, A. Wang, Y. Ran, T. Song, Y. Jiao, J. Liu, H. Zhou, W. Shi, B. He, D. Wang, Y. Li, M. Avdeev, S. Shi, *Adv. Energy Mater.* **2020**, *10*, 2001486.
- [190] J. Liu, Z. Bao, Y. Cui, E. J. Dufek, J. B. Goodenough, P. Khalifah, Q. Li, B. Y. Liaw, P. Liu, A. Manthiram, Y. S. Meng, V. R. Subramanian, M. F. Toney, V. V. Viswanathan, M. S. Whittingham, J. Xiao, W. Xu, J. Yang, X.-Q. Yang, J.-G. Zhang, *Nat. Energy* **2019**, *4*, 180.
- [191] M. Armand, J.-M. Tarascon, *nature* **2008**, *451*, 652.
- [192] W. Xu, J. Wang, F. Ding, X. Chen, E. Nasibulin, Y. Zhang, J.-G. Zhang, *Energy Environ. Sci.* **2014**, *7*, 513.
- [193] J. Peng, D. Wu, F. Song, S. Wang, Q. Niu, J. Xu, P. Lu, H. Li, L. Chen, F. Wu, *Adv. Funct. Mater.* **2022**, *32*, 2105776.
- [194] X.-B. Cheng, R. Zhang, C.-Z. Zhao, Q. Zhang, *Chem. Rev.* **2017**, *117*, 10403.
- [195] J. Kasemchainan, S. Zekoll, D. Spencer Jolly, Z. Ning, G. O. Hartley, J. Marrow, P. G. Bruce, *Nat. Mater.* **2019**, *18*, 1105.
- [196] C. Wang, Y. Gong, B. Liu, K. Fu, Y. Yao, E. Hitz, Y. Li, J. Dai, S. Xu, W. Luo, E. D. Wachsman, L. Hu, *Nano Lett.* **2017**, *17*, 565.
- [197] X. Fan, X. Ji, F. Han, J. Yue, J. Chen, L. Chen, T. Deng, J. Jiang, C. Wang, *Sci. Adv.* **2018**, *4*, aau9245.
- [198] Y. Shao, H. Wang, Z. Gong, D. Wang, B. Zheng, J. Zhu, Y. Lu, Y.-S. Hu, X. Guo, H. Li, X. Huang, Y. Yang, C.-W. Nan, L. Chen, *ACS Energy Lett.* **2018**, *3*, 1212.
- [199] W. Martin, Y. Tian, J. Xiao, *J. Electrochem. Soc.* **2021**, *168*, 060513.
- [200] M. Chandrasekar, M. Pushpavanam, *Electrochim. Acta* **2008**, *53*, 3313.
- [201] J. Xiao, Q. Li, Y. Bi, M. Cai, B. Dunn, T. Glossmann, J. Liu, T. Osaka, R. Sugiyara, B. Wu, J. Yang, J.-G. Zhang, M. S. Whittingham, *Nat. Energy* **2020**, *5*, 561.
- [202] B. Liu, J.-G. Zhang, W. Xu, *Joule* **2018**, *2*, 833.
- [203] X. Zhang, F. Ma, K. Srinivas, B. Yu, X. Chen, B. Wang, X. Wang, D. Liu, Z. Zhang, J. He, Y. Chen, *Energy Storage Mater.* **2022**, *45*, 656.
- [204] F. Ma, K. Srinivas, X. Zhang, Z. Zhang, Y. Wu, D. Liu, W. Zhang, Q. Wu, Y. Chen, *Adv. Funct. Mater.* **2022**, *32*, 2206113.
- [205] Z. Wang, X. Niu, J. Xiao, C. Wang, J. Liu, F. Gao, *RSC Adv.* **2013**, *3*, 16775.
- [206] X. Zhang, L. Zhou, K. Hu, D. Gao, S. Tang, L. He, Y. Chen, P. Zhang, Z. Zhang, *Chem. Eng. J.* **2023**, *476*, 146612.
- [207] K. L. A. Cao, T. Ogi, *Energy Storage Mater.* **2024**, *74*, 103901.
- [208] X. Cheng, C. Tang, C. Yan, J. Du, A. Chen, X. Liu, L. Jewell, Q. Zhang, *Mater. Today Nano* **2023**, *22*, 100321.
- [209] R. Liu, B. Zhang, L. Fu, Z. Fu, H. Xie, Y. Tang, H. Wang, D. Sun, *Mater. Today Chem.* **2024**, *35*, 101903.
- [210] M. Liu, F. Wu, Y. Bai, Y. Li, H. Ren, R. Zhao, X. Feng, T. Song, C. Wu, *ACS Appl. Mater. Interfaces* **2021**, *13*, 47671.
- [211] W. Luo, Y. Zhang, S. Xu, J. Dai, E. Hitz, Y. Li, C. Yang, C. Chen, B. Liu, L. Hu, *Nano Lett.* **2017**, *17*, 3792.
- [212] R. Somasundaram, T. Connelly, R. Choi, H. Choi, A. Samarkina, L. Li, E. Gregorio, Y. Chen, R. Thakur, M. Abdel-Mohsen, M. Beqiri, M. Kiernan, M. Perego, F. Wang, M. Xiao, P. Brafford, X. Yang, X. Xu, A. Secreto, G. Danet-Desnoyers, D. Traum, K. H. Kaestner, A. C. Huang, D. Hristova, J. Wang, M. Fukunaga-Kalabis, C. Krepler, F. Ping-Chen, X. Zhou, A. Gutierrez, et al., *Nat. Commun.* **2021**, *12*, 346.
- [213] W. Ye, F. Pei, X. Lan, Y. Cheng, X. Fang, Q. Zhang, N. Zheng, D.-L. Peng, M.-S. Wang, *Adv. Energy Mater.* **2020**, *10*, 1902956.
- [214] Y. Chen, Z. Wang, X. Li, X. Yao, C. Wang, Y. Li, W. Xue, D. Yu, S. Y. Kim, F. Yang, A. Kushima, G. Zhang, H. Huang, N. Wu, Y.-W. Mai, J. B. Goodenough, J. Li, *Nature* **2020**, *578*, 251.

- [215] K. Yan, Z. Lu, H.-W. Lee, F. Xiong, P.-C. Hsu, Y. Li, J. Zhao, S. Chu, Y. Cui, *Nat. Energy* **2016**, 1, 1.
- [216] X. Li, W. Ye, P. Xu, H. Huang, J. Fan, R. Yuan, M.-S. Zheng, M.-S. Wang, Q. Dong, *Adv. Mater.* **2022**, 34, 2202898.
- [217] K. Lee, Y. J. Lee, M. J. Lee, J. Han, J. Lim, K. Ryu, H. Yoon, B.-H. Kim, B. J. Kim, S. W. Lee, *Adv. Mater.* **2022**, 34, 2109767.
- [218] J. Cui, P. Su, W. Li, X. Wang, Y. Zhang, Z. Xiao, Q. An, Z. Chen, *Adv. Energy Mater.* **2025**, 2404604.
- [219] L. Yu, X. Chen, N. Yao, Y.-C. Gao, Y.-H. Yuan, Y.-B. Gao, C. Tang, Q. Zhang, *InfoMat* **2025**, 7, 12653.
- [220] Y.-W. Zhang, V. Sorkin, Z. H. Aitken, A. Politano, J. Behler, A. P. Thompson, T. W. Ko, S. P. Ong, O. Chalykh, D. Korogod, E. Podryabinkin, A. Shapeev, J. Li, Y. Mishin, Z. Pei, X. Liu, J. Kim, Y. Park, S. Hwang, S. Han, K. Sheriff, Y. Cao, R. Freitas, *Modell. Simul. Mater. Sci. Eng.* **2025**, 33, 023301.
- [221] A. P. Maltsev, I. V. Chepkasov, A. G. Kvashnin, A. R. Oganov, *Crystals* **2023**, 13, 756.
- [222] A. P. Maltsev, I. V. Chepkasov, A. R. Oganov, *ACS Appl. Mater. Interfaces* **2023**, 15, 42511.
- [223] A. V. Iosimovska, A. P. Maltsev, I. V. Chepkasov, A. R. Oganov, *Appl. Phys. Lett.* **2024**, 124, 16.
- [224] A. D. Dembitskiy, I. S. Humonen, R. A. Eremin, D. A. Aksyonov, S. S. Fedotov, S. A. Budenny, *npj Comput. Mater.* **2025**, 11, 1.
- [225] A. Merchant, S. Batzner, S. S. Schoenholz, M. Aykol, G. Cheon, E. D. Cubuk, *Nature* **2023**, 624, 80.
- [226] Y. Chen, Z. Dong, S. Lai, Y. Li, W. Lv, Y.-B. He, F. Kang, M. Liu, *Adv. Funct. Mater.* **2024**, 34, 2408657.
- [227] Z. Deng, X. Lin, Z. Huang, J. Meng, Y. Zhong, G. Ma, Y. Zhou, Y. Shen, H. Ding, Y. Huang, *Adv. Energy Mater.* **2021**, 11, 2000806.
- [228] X. Liu, Z. Liang, Y. Xiang, M. Lin, Q. Li, Z. Liu, G. Zhong, R. Fu, Y. Yang, *Adv. Mater.* **2021**, 33, 2005878.
- [229] Y. Cheng, L. Zhang, Q. Zhang, J. Li, Y. Tang, C. Delmas, T. Zhu, M. Winter, M.-S. Wang, J. Huang, *Mater. Today* **2021**, 42, 137.
- [230] Y. Zheng, L. Hu, W. Li, T. Huang, J. Ma, S. Dong, G. Cui, *ACS Energy Lett.* **2024**, 9, 5296.
- [231] Z. Sun, M. Li, B. Xiao, X. Liu, H. Lin, B. Jiang, H. Liu, M. Li, D.-L. Peng, Q. Zhang, *Etransportation* **2022**, 14, 100203.
- [232] H. Zheng, X. Lu, K. He, *J. Energy Chem.* **2022**, 68, 454.
- [233] C. Zeng, J. Liang, C. Cui, T. Zhai, H. Li, *Adv. Mater.* **2022**, 34, 2200777.
- [234] Y. Liu, Q. Li, Z. Wang, *J. Energy Chem.* **2024**, 95, 39.
- [235] X. Chen, C. Liu, Y. Fang, X. Ai, F. Zhong, H. Yang, Y. Cao, *Carbon Energy* **2022**, 4, 1133.
- [236] Y. Jiang, Z. Wang, C. Xu, W. Li, Y. Li, S. Huang, Z. Chen, B. Zhao, X. Sun, D. P. Wilkinson, J. Zhang, *Energy Storage Mater.* **2020**, 28, 17.
- [237] Y. Lu, X. Huang, Y. Ruan, Q. Wang, R. Kun, J. Yang, Z. Wen, *J. Mater. Chem. A* **2018**, 6, 18853.
- [238] R. Xu, F. Han, X. Ji, X. Fan, J. Tu, C. Wang, *Nano Energy* **2018**, 53, 958.
- [239] Y.-G. Lee, S. Fujiki, C. Jung, N. Suzuki, N. Yashiro, R. Omoda, D.-S. Ko, T. Shiratsuchi, T. Sugimoto, S. Ryu, J. H. Ku, T. Watanabe, Y. Park, Y. Aihara, D. Im, I. T. Han, *Nat. Energy* **2020**, 5, 299.



**Ilya Chepkasov** Ph.D., is a Senior Researcher in the Center for Materials Technologies at the Skolkovo Institute of Science and Technology (Skoltech). He holds a degree in Physics from Katanov Khakass State University (2010) and a Ph.D. in Condensed Matter Physics from Altai State Technical University (2013). In 2018/2019 and again in 2021, he was a visiting scientist at the Helmholtz-Zentrum Dresden-Rossendorf in Germany. He began his work at Skoltech as a Research Scientist in 2020 and was appointed to his current role as Senior Researcher in the Industry-Oriented Computational Discovery group in 2023. His expertise lies in computational materials science, specializing in molecular dynamics and ab initio methods. His research focuses on the electronic and structural properties of two-dimensional materials and nanoparticles.



**Alexander Kvashnin** is a Full Professor and the head of the Industry-Oriented Computational Discovery Lab in the Center for Materials Technologies at the Skolkovo Institute of Science and Technology (Skoltech). In 2016, Alexander received his Ph.D. in Materials Science from the National University of Science and Technology MISIS. In 2021, he successfully obtained a Habilitation degree in Materials Science. He worked as a visiting researcher at Rice University in the USA in 2011 and 2013. In 2023 Alexander was the leader of the Megagrant Laboratory "Computational Synthesis of Chemical Compounds" at the Institute of Solution Chemistry RAS. In 2023, Alexander was listed among the top 2% of the world's most cited researchers according to a single-year impact compiled by Elsevier. He actively works in the field of computational materials science investigating structure-property relations using modern computational techniques including AI. Alexander has published more than 100 research papers in high-impact journals with more than 8000 citations.